Journal of Computational Physics 315 (2016) 388–408

Contents lists available at ScienceDirect

Journal of Computational Physics

www.elsevier.com/locate/jcp

The GBS code for tokamak scrape-off layer simulations

F.D. Halpern [a,*], P. Ricci [a], S. Jolliet [a], J. Loizu [b], J. Morales [a], A. Mosetto [a], F. Musil [a], F. Riva [a], T.M. Tran [a], C. Wersal [a]

[a] Ecole Polytechnique Fédérale de Lausanne (EPFL), Swiss Plasma Center (SPC), CH-1015 Lausanne, Switzerland
[b] Max-Planck-Institut für Plasmaphysik, D-17491, Greifswald, Germany

ARTICLE INFO

Article history:
Received 5 October 2015
Received in revised form 10 March 2016
Accepted 18 March 2016
Available online 24 March 2016

Keywords:
Plasma fluid turbulence code
Tokamak scrape-off layer

ABSTRACT

We describe a new version of GBS, a 3D global, flux-driven plasma turbulence code to simulate the turbulent dynamics in the tokamak scrape-off layer (SOL), superseding the code presented by Ricci et al. (2012) [14]. The present work is driven by the objective of studying SOL turbulent dynamics in medium size tokamaks and beyond with a high-fidelity physics model. We emphasize an intertwining framework of improved physics models and the computational improvements that allow them. The model extensions include neutral atom physics, finite ion temperature, the addition of a closed field line region, and a non-Boussinesq treatment of the polarization drift. GBS has been completely refactored with the introduction of a 3-D Cartesian communicator and a scalable parallel multigrid solver. We report dramatically enhanced parallel scalability, with the possibility of treating electromagnetic fluctuations very efficiently. The method of manufactured solutions as a verification process has been carried out for this new code version, demonstrating the correct implementation of the physical model.

1. Introduction

Understanding the turbulent dynamics of the tokamak scrape-off layer (SOL) is one of the important scientific challenges to address as we approach the era of burning plasma experiments in magnetic fusion energy devices. The SOL plays a crucial role in determining the performance of tokamak devices, for instance, by controlling the impurity influx into the core plasma, the recycling level, and the heat exhaust [1]. Non-linear simulations of SOL dynamics have become an essential tool to understand transport and stability phenomena, and to interpret and develop experiments.

High-fidelity physics simulations of SOL dynamics present many modeling challenges. The problem at hand is of a multiphysics nature, involving sheath physics, neutral particles, turbulence, and, necessarily, their interaction. These phenomena take place at disparate time and spatial scales, ranging from the Larmor scale for the sheath to the machine size for the parallel structure of the turbulent structures. Experimental measurements have highlighted the fundamental aspects of the strong turbulent dynamics that must be retained, with high amplitude modes that have a radial extension similar to the SOL gradient length, $L_p = -p/\nabla p \sim 1$ cm [2]. Plasma transport is intermittent, i.e. the fluctuation probability distribution functions are skewed, and therefore a purely diffusive approach is in principle insufficient to describe plasma profile evolution.

* Corresponding author.
E-mail address: federico.halpern@epfl.ch (F.D. Halpern).

http://dx.doi.org/10.1016/j.jcp.2016.03.040
0021-9991/

In the past decade, computational models have increased our understanding of SOL dynamics. The fluctuation levels and intermittency found in the tokamak SOL were first recovered using 2D fluid turbulence codes such as TOKAM2D, ESEL, and SOLT [3–7], where the fluid equations are integrated along the direction parallel to the magnetic field lines and closed by using assumptions on the losses at the end of the field lines. The fluid approach is justified by the large collisionality in the SOL, where the plasma temperature is a few tens of electronvolts, and by the low frequency and wavenumber of the turbulence. These codes included the physics of blob filaments [8] and of curvature-driven modes in the absence of parallel dynamics. However, 3D effects such as drift-wave turbulence and magnetic fluctuations can have a strong impact on edge turbulence [9]. Advances in computer hardware and algorithms have now enabled the study of SOL dynamics in 3D using codes such as GEMR [9,10], BOUT++ [11], TOKAM3D/3X [12,13], and GBS [14].

The present paper describes a new version of the GBS code, a 3D global, flux-driven, two-fluid turbulence code implemented using finite differences for the spatial discretization and traditional Runge–Kutta methods for the time advance. GBS was originally developed as a 2D code to simulate the turbulent dynamics of field-aligned turbulence in basic plasma physics devices such as TORPEX [15,16]. The numerical approach used was similar to that of the TOKAM2D, ESEL, and SOLT codes, e.g. with the use of explicit or semi-implicit time marching algorithms and the Arakawa scheme [17] to treat non-linear $\mathbf{E} \times \mathbf{B}$ advection terms.

In recent years, GBS was generalized to 3D, effectively adding ballooning, drift-wave, sheath physics, and electromagnetic fluctuations. The parallel dynamics was treated using field-aligned parallel gradient operators based on centered finite differences. The resulting algorithm, while lightweight and fairly robust, required the magnetic safety factor q to be a radially constant rational number. A description of this code was published in [14]. Magnetic shear effects were implemented using the $\hat{s} - \alpha$ metric coefficients [18], and then updated to include finite aspect ratio effects [19]. The numerical approach for the parallel gradient was recently generalized to allow varying q [20].

A new version of GBS, presented herein, has been developed with the specific goal of studying the SOL dynamics of medium size tokamaks using high fidelity, realistic-size global turbulence simulations. This involves resolving scales from the order of the ion sound Larmor gyroradius, $\rho_s \lesssim 1$ mm ($\rho_s = c_s/\omega_{ci} = \sqrt{T_e/m_i}/(eB/m_i)$) up to the machine size $R \sim 1$ m, including ion temperature dynamics [21], neutral particle physics [22], and a full treatment of the polarization drift avoiding the Boussinesq approximation. The largest GBS simulations carried out so far reproduced the SOL dynamics of TCV [23] or Alcator C-Mod [24] with $\rho_*^{-1} = R/\rho_s \approx 2000$. We also introduce a closed field line region, as a means to represent the particle and heat outflow into the SOL more realistically.

As it will be shown, one of the main computational obstacles to reach the plasma size of TCV or C-Mod is the inversion of the Poisson and Ampère operators, since standard sparse matrix-based methods perform poorly as the problem size increases. We report that the sparse solvers are now superseded by a stencil-based, parallel multigrid solver. The use of an iterative solver has the added benefit, respect to direct solvers, that time varying operators can be treated in a computationally efficient manner. This has allowed the removal of the Boussinesq approximation from the vorticity equation. Additionally, simulations with electromagnetic fluctuations can now be carried out with only a small increase in computational cost at any plasma size.

The paper is organized as follows. First, in Section 2 we present the complete physical model used to describe the SOL dynamics, including neutral atom physics and a more rigorous, non-Boussinesq description of the polarization velocity. Then, in Section 3 we discuss computational details of the GBS implementation, such as the rigorous code verification procedure employed, the neutral physics module, the parallel multigrid solver, and we demonstrate improved parallel scalability of the GBS code. Examples of the application of the new GBS code follow in Section 4. Some final remarks on this work can be found in Section 5.

2. Physical model for scrape-off layer dynamics

The philosophy behind the development of GBS is to approach a very complex problem, such as tokamak edge turbulent dynamics, in steps of increasing complexity. This method effectively reduces the problem into more tractable parts, and facilitates the interpretation of both simulation results and experimental measurements. Consequently, the first 3D version of GBS employed a cold-ion version of the two-fluid drift-reduced Braginskii equations [25], aiming at explaining turbulence in basic plasma physics devices with a simple geometry and where typically only electron heating is available.

In effect, the first turbulent studies in 3D using GBS involved linear devices such as LAPD, which have turbulent modes in a straight open magnetic field line configuration [26,27]. Then, curvature driven (interchange) modes and seeded plasma filament dynamics where studied in simulations of the TORPEX device, where the superposition of toroidal and vertical magnetic fields gives rise to helicoidal field lines [15,28–32]. This required a description of the parallel dynamics in the presence of vertically tilted magnetic field lines.

A toroidal limiter tokamak geometry became available in GBS around 2010, with the first results being the identification of the turbulent saturation mechanisms [33]. A complete set of boundary conditions for all fluid moments was derived [34]. Then, several papers describing the turbulent dynamics in this geometry followed, concentrating on identifying the linear and non-linear turbulent regimes [35,36], the equilibrium electric field, the intrinsic toroidal plasma flows, and the effect of the limiter position [37–39]. Much of the research focus has been on clarifying the physical mechanisms setting the SOL width [40–42]. More recently, a detailed comparison of GBS simulations with Gas Puff Imaging (GPI) data of Alcator C-Mod

inner-wall limited discharges [43] was carried out, finding that the observed turbulence characteristics and the background profiles are very well reproduced in the simulations [44].

GBS SOL simulations follow the plasma dynamics within an annular region with right-handed coordinates $(y = a\theta, x, \varphi)$, which represent the poloidal length around the minor radius a, the radius, and the toroidal angle. The toroidal coordinate φ is periodic, while periodicity in y can be selected for a given range of x. The periodic region corresponds to the closed flux-surface region, while the SOL extends outside the last closed flux-surface where the magnetic field lines are not periodic. A toroidal limiter can be placed at an arbitrary poloidal angle. Simulations involve localized density and temperature source terms (close to and at the inner boundary of the simulated domain) building up the profiles in time, which then drives the turbulence. This is the so-called "flux-driven" approach. Our turbulence studies focus on the steady state regime where plasma injection, turbulent transport, and losses at the limiter balance each other. The recently introduced closed field-line region allows sources to be placed inside the confined region, driving turbulence and allowing the outflowing turbulent structures to fill the SOL with plasma.

In the following subsections, we provide a complete description of the simulation model. We start with the fluid moments for the main plasma species, including the effects of neutrals, in section 2.1. This is followed by a discussion of the drift-reduction procedure, leading to the final model equations 2.2. The boundary conditions for the plasma-wall interface are described in section 2.3, while the kinetic model for neutral particle physics is shown in section 2.4. A description of the fluid equations follows below.

2.1. Main plasma species model equations

The derivation of the fluid equations starts from the Boltzmann equations for the ion and electron species, where we include Krook collision operators describing the interaction of ions and electrons with neutrals. These neutral particles interact with the main plasma species through collisional processes, and play an important role in the SOL dynamics, in particular, regulating the heat and particle fluxes to the first wall. For the ion species we consider ionization, recombination, and charge-exchange processes, while for the electrons, we consider ionization, recombination, and elastic collision processes. The kinetic equations considered are

$$\frac{\partial f_i}{\partial t} + \mathbf{v}\cdot\frac{\partial f_i}{\partial \mathbf{x}} + \mathbf{a}_i\cdot\frac{\partial f_i}{\partial \mathbf{v}} = \nu_{\mathrm{iz}} f_{\mathrm{n}} - \nu_{\mathrm{cx}}\left(\frac{n_{\mathrm{n}}}{n_i} f_i - f_{\mathrm{n}}\right) - \nu_{\mathrm{rec}} f_i + C_i(f_e, f_i), \tag{1}$$

$$\frac{\partial f_e}{\partial t} + \mathbf{v}\cdot\frac{\partial f_e}{\partial \mathbf{x}} + \mathbf{a}_e\cdot\frac{\partial f_e}{\partial \mathbf{v}} = \nu_{\mathrm{iz}} n_{\mathrm{n}}\left[2\Phi_e(\mathbf{v}_{\mathrm{n}}, T_{e,\mathrm{iz}}) - \frac{f_{\mathrm{e}}}{n_{\mathrm{e}}}\right] + \nu_{\mathrm{en}} n_{\mathrm{n}}\left[\Phi_e(\mathbf{v}_{\mathrm{n}}, T_{e,\mathrm{en}}) - \frac{f_e}{n_e}\right] - \nu_{\mathrm{rec}} f_e + C_e(f_e, f_i) \tag{2}$$

where $\mathbf{a}_{e,i} = Z_{e,i} e(\mathbf{E} + \mathbf{v}_{e,i}\times\mathbf{B})/m_{e,i}$ is the particle acceleration due to the Lorentz force, Φ_e is a Maxwellian distribution function for electrons with an average velocity equal to the local average neutral velocity, and temperatures $T_{e,iz} = T_e/2 - E_{iz}/3 + m_e v_e^2/6 - m_e v_n^2/3$ and $T_{e,en} = T_e + m_e(v_e^2 - v_n^2)/3$ depending on local plasma and neutral properties to ensure energy conservation in the high mass ratio limit [22]. E_{iz} is the ionization energy, and C_i and C_e are the Coulomb collision operators including both inter- and intra-species collisions for ions and electrons respectively. The subscripts $\{e, i, \mathrm{n}\}$ denote, respectively, electrons, ions, and neutrals.

The ionization, recombination, elastic electron–neutral, and charge-exchange processes are described, respectively, through the use of Krook operators with collision frequencies defined as

$$\nu_{\mathrm{iz}} = n_e\langle v_e \sigma_{\mathrm{iz}}(v_e)\rangle \tag{3}$$

$$\nu_{\mathrm{rec}} = n_e\langle v_e \sigma_{\mathrm{rec}}(v_e)\rangle \tag{4}$$

$$\nu_{\mathrm{en}} = n_e\langle v_e \sigma_{\mathrm{en}}(v_e)\rangle \tag{5}$$

$$\nu_{\mathrm{cx}} = n_i\langle v_i \sigma_{\mathrm{cx}}(v_i)\rangle \tag{6}$$

where σ_{iz}, σ_{rec}, σ_{en} and σ_{cx}, are the ionization, recombination, elastic electron–neutral, and charge-exchange cross sections. The effective reaction rates, $\langle v\sigma\rangle$, are taken from the OpenADAS [45][1] database.

The fluid equations result from the first three moments of the kinetic equations in the Braginskii limit. We consider the limit where the neutral collision times are much larger than the Coulomb collision times, which allows us to retain the Braginskii closure for the ion and electron species [46]. In the case where the neutral and Coulomb collision times cannot be separated, a different closure procedure is required [47]. More sophisticated limits for the fluid equations, such as the general gyroviscous expression for the main ion species [48], are left for future work. The Braginskii moment equations, including terms describing interactions between the main plasma species and the neutrals, are given by

[1] OpenADAS – http://open.adas.ac.uk.

$$\frac{\partial n_e}{\partial t} = -\nabla\cdot(n_e\mathbf{v}_e) + n_{\rm n}\nu_{\rm iz} - n_i\nu_{\rm rec} + S_n \tag{7}$$

$$\frac{\partial n_i}{\partial t} = -\nabla\cdot(n_i\mathbf{v}_i) + n_{\rm n}\nu_{\rm iz} - n_i\nu_{\rm rec} + S_n \tag{8}$$

$$\begin{aligned} m_e n_e \frac{\mathrm{d}_e\mathbf{v}_e}{\mathrm{d}t} &= -\nabla p_e - \nabla\cdot\Pi_e - en_e\left[\mathbf{E}+\mathbf{v}_e\times\mathbf{B}\right] + \mathbf{R}_{ei} \\ &\quad + m_e n_{\rm n}(\nu_{\rm en}+2\nu_{\rm iz})(\mathbf{v}_{\rm n}-\mathbf{v}_e) \end{aligned} \tag{9}$$

$$\begin{aligned} m_i n_i \frac{\mathrm{d}_i\mathbf{v}_i}{\mathrm{d}t} &= -\nabla p_i - \nabla\cdot\Pi_i + Z_i e n_i\left[\mathbf{E}+\mathbf{v}_i\times\mathbf{B}\right] - \mathbf{R}_{ei} \\ &\quad + m_i n_{\rm n}(\nu_{\rm iz}+\nu_{\rm cx})(\mathbf{v}_{\rm n}-\mathbf{v}_i) \end{aligned} \tag{10}$$

$$\begin{aligned} \frac{3}{2}n_e\frac{\mathrm{d}_e T_e}{\mathrm{d}t} &= -p_e\nabla\cdot\mathbf{v}_\mathbf{e} - \nabla\cdot\mathbf{q}_e - \Pi_e:\nabla\mathbf{v}_e + Q_e \\ &\quad + n_{\rm n}\nu_{\rm iz}\left[-E_{\rm iz} - \frac{3}{2}T_e + \frac{3}{2}m_e\mathbf{v}_e\cdot\left(\mathbf{v}_e - \frac{4}{3}\mathbf{v}_{\rm n}\right)\right] \\ &\quad - n_{\rm n}\nu_{\rm en}m_e\mathbf{v}_e\cdot(\mathbf{v}_{\rm n}-\mathbf{v}_e) + \frac{3}{2}n_e S_{T_e} \end{aligned} \tag{11}$$

$$\begin{aligned} \frac{3}{2}n_i\frac{\mathrm{d}_i \mathrm{T}_i}{\mathrm{d}t} &= -p_i\nabla\cdot\mathbf{v}_\mathbf{i} - \nabla\cdot\mathbf{q}_i - \Pi_i:\nabla\mathbf{v}_i + Q_i \\ &\quad + n_{\rm n}(\nu_{\rm iz}+\nu_{\rm cx})\left[\frac{3}{2}(T_{\rm n}-T_i) + \frac{m_i}{2}(\mathbf{v}_{\rm n}-\mathbf{v}_i)^2\right] + \frac{3}{2}n_i S_{T_i}, \end{aligned} \tag{12}$$

where $\Pi_{e,i}$ are the stress tensors, $E_{\rm iz}$ is the ionization energy, $\mathbf{R}_{ei}$ is the friction force between electrons and ions, $p_{e,i}$ is the pressure, $\mathbf{q}_{e,i}$ is the heat flux density, and Q is the heat generated by Coulomb collisions. The definitions of the stress tensor, heat fluxes and sources, and friction forces used are given in the review by Braginskii [46].

The detailed derivation of the terms describing the interaction between plasma and neutrals can be found in [22]. These terms consist of plasma sources and sinks due to ionization and recombination processes, in Eqs. (7) and (8); an explicit electron energy sink to accommodate for the ionization energy, in Eq. (11); the drag and equipartition terms due to the difference between the neutral and plasma particle velocity and temperature, in Eqs. (9)–(12); and the heat generated by friction between the plasma and the neutral species, in Eqs. (11) and (12).

2.2. Drift reduced equations

Although much simpler than the kinetic equations, the fluid moment equations still contains temporal scales (e.g. ω_c^{-1}) that are typically not of interest for modeling turbulent dynamics. Additionally, we observe that the perpendicular (turbulent) dynamics occur in length scales of the order of ρ_s, while the relevant length scale for the parallel dynamics is the magnetic field line length $\sim R$. Hence, it is advantageous to eliminate the undesired (fast) temporal scales, and to separate the parallel and the perpendicular dynamics. The required separation of temporal and spatial scales is achieved through the use of the following velocity representation:

$$\mathbf{v}_e = v_{\parallel e}\hat{\mathbf{b}} + \mathbf{v}_{\mathbf{E}\times\mathbf{B}} + \mathbf{v}_{\star,e} \tag{13}$$

$$\mathbf{v}_i = v_{\parallel i}\hat{\mathbf{b}} + \mathbf{v}_{\mathbf{E}\times\mathbf{B}} + \mathbf{v}_{\star,i} + \mathbf{v}_{{\rm pol},i} \tag{14}$$

together with the approximation $\mathbf{E} = -\nabla\phi - \hat{\mathbf{b}}_0\partial_t\psi$, where ψ represents the perturbed poloidal magnetic flux. The drift velocities $\mathbf{v}_{\mathbf{E}\times\mathbf{B}} = -\nabla\phi\times\hat{\mathbf{b}}_0/B$ and $\mathbf{v}_{\star,e,i} = -\nabla p_{e,i}\times\hat{\mathbf{b}}_0/(Z_{e,i}en_{e,i}B)$ are the zeroth order solution to the perpendicular component of equations (9) and (10). Here $\hat{\mathbf{b}}$ is a unit vector in the direction of the magnetic field, with an equilibrium component $\hat{\mathbf{b}}_0$. The ion polarization drift $\mathbf{v}_{{\rm pol},i}$ is obtained as a first order correction to the solution of equation (10), using $\mathbf{v}_{\mathbf{E}\times\mathbf{B}} + \mathbf{v}_{\star,i}$ as an estimate for $\mathbf{v}_i$:

$$\mathbf{v}_{{\rm pol},i} \approx -\frac{1}{n_i\omega_{ci}}\frac{\mathrm{d}_i}{\mathrm{d}t}\left(\frac{n_i}{B}\nabla_\perp\phi + \frac{1}{eB}\nabla_\perp p_i\right) + \frac{1}{m_i n_i\omega_{ci}}\hat{\mathbf{b}}_0\times\left[G_i\kappa - \frac{\nabla G_i}{3}\right]. \tag{15}$$

The magnetic field line curvature vector is given by $\kappa = \hat{\mathbf{b}}_0\cdot\nabla\hat{\mathbf{b}}_0$, and, after imposing $\frac{d}{dt} \ll \omega_{ci}$, only the viscous component of the ion stress function is retained:

$$G_i = -\eta_{0i}\left(2\nabla_\parallel v_{\parallel i} + \frac{\hat{C}(\phi)}{B} + \frac{\hat{C}(p_i)}{Z_i e n_i B}\right). \tag{16}$$

Here $\eta_{0i} = n_i T_i\tau_{ie}$ is the viscous coefficient (τ_{ie} is the electron–ion collision time), and the curvature operator is defined as $\hat{C}(a) = (B/2)\left[\nabla\times(\hat{\mathbf{b}}_0/B)\right]\cdot\nabla a$. In GBS, the polarization velocity (equation (15)) and its divergence retain corrections due to

Table 1
Normalizations and dimensionless parameters used in GBS.

Primitive variables		
Quantity	Unit	Definition
B_0	T	Magnetic field at the magnetic axis
n_{e0}	m^{-3}	Density at the LCFS
T_{e0}	eV	Temperature at the LCFS
R_0	m	Major radius at the magnetic axis

Gyrobohm normalizations		
Quantity	Definition	
c_{s0}	$\sqrt{T_{e0}/m_i}$	Sound speed
ω_{ci0}	eB_0/m_i	Ion gyrofrequency
ρ_{s0}	$c_{s0}\omega_{ci0}$	Ion sound Larmor gyroradius

Time and space normalizations		
Quantity	Normalization	Definition
$l_\perp$	ρ_{s0}	Reference perpendicular length
$l_\parallel$	R_0	Reference parallel length
t	R/c_{s0}	Reference time

Dimensionless variables		
Parameter	Normalization	Definition
n	n_{e0}	Density
ϕ	T_{e0}/e	Electric potential
Ω	$n_{e0}T_{e0}/(e\rho_{s0}^2)$	Vorticity
$v_{\parallel e,i}$	c_{s0}	Electron/ion parallel velocities
$T_{e,i}$	$T_{(e,i)0}$	Electron/ion temperatures
ψ	$2m_ic_{s0}/(e\beta_{e0})$	Poloidal magnetic flux

Dimensionless parameters		
Parameter	Definition	
ν	$en_{e0}R_0/(m_ic_{s0}\sigma_\parallel)$	Dimensionless Spitzer resistivity
$\rho_\star$	ρ_{s0}/R_0	Normalized ion sound Larmor gyroradius
β_{e0}	$2\mu_0 n_{e0}T_{e0}/B_0^2$	Electron plasma beta
τ	T_{i0}/T_{e0}	Temperature ratio

Diffusion coefficients		
Parameter	Normalization	
$D, \chi_\perp$	$c_{s0}\rho_{s0}^2/R_0$	Particle/heat diffusion coefficients
$\chi_\parallel$	$c_{s0}R_0$	Parallel heat diffusion coefficient

density gradients, i.e. we avoid the commonly used Boussinesq approximation by recasting equation (10) as an equation for the momentum before carrying out the drift reduction. The derivation of the polarization velocity and its divergence, which are somewhat lengthy, are condensed in Appendix A. The equations are similar to those found by Simakov and Catto [49,50].

Once the polarization velocity and its divergence are known, obtaining the drift reduced equations is straightforward. The principal idea is to expand equations (7)–(12) using equations (13) and (14). Assuming a quasi-neutral plasma, we retain an equation for the electron density, a vorticity equation that enforces charge conservation, and equations for the ion and electron parallel velocities and temperatures. We use the charge number $Z_i = 1$ for the main ion species. The drift-reduced equations implemented in GBS are given below, using the normalized units, symbols, and dimensionless plasma parameters defined in Table 1. These normalized units are used throughout the rest of the paper.

$$\frac{\partial n}{\partial t} = -\frac{\rho_\star^{-1}}{B}\{\phi, n\} - \nabla\cdot\left(nv_{\parallel e}\hat{\mathbf{b}}\right) + \frac{2}{B}\left[n\hat{C}(T_e) + T_e\hat{C}(n) - n\hat{C}(\phi)\right] + D_n\nabla_\perp^2 n + S_n + \nu_{\mathrm{iz}}n_{\mathrm{n}} - n_i\nu_{\mathrm{rec}} \tag{17}$$

$$\frac{\partial \Omega}{\partial t} = -\frac{\rho_\star^{-1}}{B}\nabla_\perp\cdot\{\phi,\omega\} - \nabla_\perp\cdot\left[\nabla_\parallel(v_{\parallel i}\omega)\right] + \frac{B}{3}\hat{C}(G_i) + B^2\nabla\cdot\left(j_\parallel\hat{\mathbf{b}}\right) + 2B\hat{C}(p_e + \tau p_i) + D_\Omega\nabla_\perp^2\Omega - \frac{n_{\mathrm{n}}}{n}\nu_{\mathbf{cx}}\Omega \tag{18}$$

$$\frac{\partial U_{\parallel e}}{\partial t} = -\frac{\rho_\star^{-1}}{B}\left\{\phi, v_{\parallel e}\right\} - v_{\parallel e}\nabla_\parallel v_{\parallel e}$$

$$+\frac{m_i}{m_e}\left[\frac{\nu j_\parallel}{n}+\nabla_\parallel\phi-\frac{\nabla_\parallel p_e}{n}-0.71\nabla_\parallel T_e-\frac{2}{3n}\nabla_\parallel G_e\right]$$
$$+D_{v_{\parallel e}}\nabla_\perp^2 v_{\parallel e}+\frac{n_\mathrm{n}}{n}\left(\nu_\mathrm{en}+2\nu_\mathrm{iz}\right)\left(v_{\parallel\mathrm{n}}-v_{\parallel e}\right) \tag{19}$$

$$\frac{\partial v_{\parallel i}}{\partial t}=-\frac{\rho_\star^{-1}}{B}\left\{\phi,v_{\parallel i}\right\}-v_{\parallel i}\nabla_\parallel v_{\parallel i}-\frac{2}{3n}\nabla_\parallel G_i-\frac{1}{n}\nabla_\parallel\left(p_e+\tau p_i\right)$$
$$+D_{v_{\parallel i}}\nabla_\perp^2 v_{\parallel i}+\frac{n_\mathrm{n}}{n}\left(\nu_\mathrm{iz}+\nu_\mathrm{cx}\right)\left(v_{\parallel\mathrm{n}}-v_{\parallel i}\right) \tag{20}$$

$$\frac{\partial T_e}{\partial t}=-\frac{\rho_\star^{-1}}{B}\left\{\phi,T_e\right\}-v_{\parallel e}\nabla_\parallel T_e+\frac{4}{3}\frac{T_e}{B}\left[\frac{7}{2}\hat{C}(T_e)+\frac{T_e}{n}\hat{C}(n)-\hat{C}(\phi)\right]$$
$$+\frac{2}{3}\left\{T_e\left[0.71\nabla\cdot\left(v_{\parallel i}\hat{\mathbf{b}}\right)-1.71\nabla\cdot\left(v_{\parallel e}\hat{\mathbf{b}}\right)\right]+0.71T_e(v_{\parallel i}-v_{\parallel e})\frac{\nabla_\parallel n}{n}\right\}$$
$$+\chi_{\perp,e}\nabla_\perp^2 T_e+\nabla_\parallel\left(\chi_{\parallel,e}\nabla_\parallel T_e\right)+S_{T_e}-\frac{n_\mathrm{n}}{n}\nu_\mathrm{en}m_\mathrm{e}\frac{2}{3}v_{\parallel e}(v_{\parallel\mathrm{n}}-v_{\parallel e})$$
$$+\frac{n_\mathrm{n}}{n}\nu_\mathrm{iz}\left[-\frac{2}{3}E_\mathrm{iz}-T_\mathrm{e}+m_\mathrm{e}v_{\parallel\mathrm{e}}\left(v_{\parallel\mathrm{e}}-\frac{4}{3}v_{\parallel\mathrm{n}}\right)\right] \tag{21}$$

$$\frac{\partial T_i}{\partial t}=-\frac{\rho_\star^{-1}}{B}\left\{\phi,T_i\right\}-v_{\parallel i}\nabla_\parallel T_i+\frac{4}{3}\frac{T_i}{B}\left[\hat{C}(T_e)+\frac{T_e}{n}\hat{C}(n)-\hat{C}(\phi)\right]$$
$$+\frac{2}{3}T_i\left(v_{\parallel i}-v_{\parallel e}\right)\frac{\nabla_\parallel n}{n}-\frac{2}{3}T_i\nabla\cdot\left(v_{\parallel e}\hat{\mathbf{b}}\right)-\frac{10}{3}\frac{T_i}{B}\hat{C}(T_i)$$
$$+\chi_{\perp,i}\nabla_\perp^2 T_i+\nabla_\parallel\left(\chi_{\parallel,i}\nabla_\parallel T_i\right)+S_{T_i}$$
$$+\frac{n_\mathrm{n}}{n}(\nu_\mathrm{iz}+\nu_\mathrm{cx})\left[T_\mathrm{n}-T_\mathrm{i}+\frac{1}{3}(v_{\parallel\mathrm{n}}-v_{\parallel\mathrm{i}})^2\right]. \tag{22}$$

We make use of the following definitions: the Poisson bracket is $\{a,b\}=\hat{\mathbf{b}}_0\cdot(\nabla a\times\nabla b)$, the scalar vorticity is $\Omega=\nabla\cdot\omega=\nabla\cdot(n\nabla_\perp\phi+\tau\nabla_\perp p_i)$, $j_\parallel=n\left(v_{\parallel i}-v_{\parallel e}\right)$ is the parallel current, and $U_{\parallel e}=v_{\parallel e}+\beta_{e0}m_i\psi/(2m_e)$ is the sum of electron inertial and electromagnetic flutter contributions. In fact, ψ is related to the (dynamically induced) magnetic field through the expression $\mathbf{B}_1=-\beta_{e0}\nabla\times(\psi\hat{\mathbf{b}}_0)/2$. The unit magnetic field vector can then be defined as $\hat{\mathbf{b}}=\hat{\mathbf{b}}_0+\mathbf{B}_1/B$. It can be shown that $\mathbf{B}_1\perp\mathbf{B}_0$, which in fact excludes the fast compressional Alfvén wave from the dynamics. Including the electromagnetic flutter contribution, the parallel derivative is given by $\nabla_\parallel a=\hat{\mathbf{b}}_0\cdot\nabla a+\beta_{e0}\{\psi,a\}/(2B\rho_\star)$.

The source terms S_n, S_{T_e}, and S_{T_i} have been added to the density and temperature equations to model the outflow of hot plasma from the core to the SOL. These sources are poloidally and toroidally constant, and Gaussian shaped in the radial direction. They are localized in a narrow radial domain inside the closed field line region. In simulations including only the SOL, the position of the source defines the last closed flux surface (LCFS).

In normalized form, the gyroviscous terms are given by

$$G_i=-\eta_{0i}\left(2\nabla_\parallel v_{\parallel i}+\frac{\hat{C}(\phi)}{B}+\frac{\hat{C}(p_i)}{nB}\right) \tag{23}$$

$$G_e=-\eta_{0e}\left(2\nabla_\parallel v_{\parallel e}+\frac{\hat{C}(\phi)}{B}-\frac{\hat{C}(p_e)}{nB}\right). \tag{24}$$

Originally, small constant coefficients $\eta_{0e,i}$ were used in GBS to avoid numerical pile-up at high parallel wavenumbers, effectively damping modes whose wavelengths are too short to be resolved by the numerical grid. With the various improvements of the code, these coefficients can now be assigned their physical values. A similar approach is used for the parallel heat flux terms. The parallel heat diffusion coefficients, $\chi_{\parallel e,i}$, used to be set to a constant, but alternatively they can have the form $\chi_{\parallel e,i}\propto T_{i,e}^{5/2}$ now.

The simulation model makes extensive use of the auxiliary scalar functions ϕ, $v_{\parallel e}$, and ψ, which must be extracted from the dynamical (e.g. left-hand side) variables Ω and $U_{\parallel e}$ by inverting the following generalized Poisson and Ampère equations:

$$\nabla\cdot(n\nabla_\perp\phi)=\Omega-\tau\nabla_\perp^2 p_i \tag{25}$$

$$\left(\nabla_\perp^2-\frac{\beta_{e0}}{2}\frac{m_i}{m_e}n\right)v_{\parallel e}=\nabla_\perp^2 U_{\parallel e}-\frac{\beta_{e0}}{2}\frac{m_i}{m_e}nv_{\parallel i}, \tag{26}$$

with the magnetic flux deduced from

$$\psi = \left(U_{\parallel e} - v_{\parallel e}\right)\left(\frac{\beta_{e0}}{2}\frac{m_i}{m_e}\right)^{-1}. \tag{27}$$

The electrostatic potential, thus, involves corrections arising from the density gradient, which should not be neglected in the SOL where the fluctuations are $\mathcal{O}(1)$. Additionally, there is a shielding term on the right hand side of equation (25), $\sim \tau k_\perp^2 p_i$. Equation (26) reverts to $U_{\parallel e} = v_{\parallel e}$ in the pure electrostatic case. Finally, we remark here that the Poisson and Ampère operators are time evolving. Thus, obtaining a solution to equations (25) and (26) through standard sparse methods involves rebuilding and reinverting the operators every timestep. This is impractical due to the excessive computational cost. We developed a stencil-based multigrid solver to invert these operators efficiently, which is detailed in section 3. The GBS model (equations (17)–(27)) is closed by a set of generalized Bohm–Chodura boundary conditions applied at the entrance of the magnetic presheath, as described below.

2.3. Boundary conditions

As GBS has been used to model turbulence in open magnetic field line configurations, major efforts have been placed in describing the interface between the plasma and the vacuum vessel. The treatment of the Bohm–Chodura sheath is crucial and therefore we describe its implementation. The boundary conditions were first derived in [34], with corrections for finite T_i introduced in [21]. Following these papers, we generalize the boundary conditions to relax the Boussinesq approximations.

When a plasma touches a wall, a plasma sheath contiguous to the wall is formed. Within the sheath layer, both ions and electrons are accelerated by large electric fields, the drift approximation breaks down, and eventually the plasma becomes non-neutral. In the case where the plasma flows along magnetic fields that are incident to the wall at an oblique angle, three distinct sheath regions can be identified as the wall is approached [51]. First comes the collisional presheath, where ions remain magnetized and the plasma is ambipolarly accelerated in the parallel direction. Then comes the magnetic presheath (MP), which remains quasi-neutral but where the drift-approximation breaks down due to a large electric field established on the ρ_s scale and in the direction normal to the wall surface. The MP is followed by the Debye sheath, where an even larger electric field is established on the Debye length scale and where quasi-neutrality is not satisfied. Therefore, boundary conditions for the drift-fluid equations, Eqs. (17)–(27), describing the proper sheath physics are required at the MP entrance.

Here, we outline the principal steps leading to a generalized set of Bohm–Chodura sheath boundary conditions for all the fluid fields. The steady-state dynamics of the plasma is analyzed in the collisional presheath, where the drift-Braginskii model still applies. Moreover, in the vicinity of the MP entrance, the sheath electric field is so strong that plasma gradients in the direction normal to the wall become dominant. Thus, the system of fluid equations becomes, in first approximation, one dimensional, and can be greatly simplified by keeping only terms that contain gradients in the direction normal to the wall. In the infinite aspect ratio limit, the direction normal to the wall is aligned to the GBS coordinate y. The effect of radial gradients can also be considered and gives rise to corrections due to $\mathbf{E}\times\mathbf{B}$ and diamagnetic drifts. Under these assumptions, the steady-state Braginskii equations can be written as a linear system of equations of the form $\mathbf{MX} = \mathbf{S}$, where $\mathbf{X} = \left[\partial_y n, \partial_y v_{\parallel i}, \partial_y \phi, \partial_y T_e, \partial_y T_i\right]$, $\mathbf{M}$ is a matrix that depends on local quantities, and $\mathbf{S}$ represents the source of particles, momentum, and heat.

As the MP is reached, gradients in the y direction become large. However, the intensity of the sources does not necessarily change, thus the terms in $\mathbf{MX}$ balance each other and are much larger than the source terms. We approximate this as $\mathbf{MX} \approx 0$, which requires that $\det(\mathbf{M}) = 0$ is satisfied. This defines the entrance of the MP, and, imposing this condition, one obtains the value of the ion velocity at the MP entrance. Finally, from the matrix system $\mathbf{MX} \approx 0$ one can obtain relations between the plasma gradients at the MP entrance, leading to a complete set of boundary conditions. The boundary condition for $v_{\parallel e}$ must be derived from a kinetic theory [34]. The final result is

$$v_{\parallel i} = \sqrt{T_e}\left(\pm\sqrt{F_T} + \theta_n - \frac{\theta_T}{2} - \frac{2\phi}{T_e}\theta_\phi\right) \tag{28}$$

$$v_{\parallel e} = \sqrt{T_e}\left(\pm\exp\left(\Lambda - \frac{\phi}{T_e}\right) - \frac{2\phi}{T_e}\theta_\phi + 2\left(\theta_n + \theta_{T_e}\right)\right) \tag{29}$$

$$\frac{\partial n}{\partial y} = -\frac{n}{\sqrt{T_e}}\left(\pm\frac{1}{\sqrt{F_T}} + \frac{\theta_n}{F_T} + \frac{\theta_T}{2F_T}\right)\frac{\partial v_{\parallel i}}{\partial y} \tag{30}$$

$$\frac{\partial \phi}{\partial y} = -\sqrt{T_e}\left(\pm\frac{1}{\sqrt{F_T}} + \frac{\theta_n}{F_T} + \frac{\theta_T}{2F_T}\right)\frac{\partial v_{\parallel i}}{\partial y} \tag{31}$$

$$\Omega = -\left(nF_T\cos^2\chi\right)\times\left[\left(\pm\frac{\theta_{F_T}}{F_T^{3/2}} - \frac{2\theta_T}{F_T^{3/2}} - \frac{2\theta_n}{F_T^{3/2}}\right)\left(\frac{\partial v_{\parallel i}}{\partial y}\right)^2 + \sqrt{T_e}\left(\pm\frac{1}{\sqrt{F_T}} + \frac{\theta_n}{F_T} + \frac{\theta_T}{2F_T}\right)\frac{\partial^2 v_{\parallel i}}{\partial y^2}\right] \tag{32}$$

$$\frac{\partial T_e}{\partial y} \approx 0 \tag{33}$$

$$\frac{\partial T_i}{\partial y} \approx 0 \tag{34}$$

In the above expressions, all quantities are given at the magnetic presheath entrance, $F_T = 1 + \tau T_i/T_e$, and the $\pm$ signs indicates values at opposite ends of the field lines. We find that the largest contribution to $\Omega \sim (\partial_y v_{\|i})^2/F_T$ in the Boussinesq boundary conditions [34] cancels out exactly with a non-Boussinesq contribution. The temperature gradients along y are very small and can be neglected, since one finds that $\partial_y T_e \sim \partial_y T_i \approx 0.1\partial_y \phi$ [34,21]. The drift corrections arising from radial plasma gradients are defined as follows:

$$\theta_n = \frac{\sqrt{T_e}}{2\tan\chi}\frac{\partial \ln n}{\partial r} \tag{35}$$

$$\theta_{T_e} = \frac{\sqrt{T_e}}{2\tan\chi}\frac{\partial \ln T_e}{\partial r} \tag{36}$$

$$\theta_T = \frac{\sqrt{T_e}}{2\tan\chi}\frac{\partial \ln (F_T T_e)}{\partial r} \tag{37}$$

$$\theta_{F_T} = \frac{\sqrt{T_e}}{2\tan\chi}\frac{\partial \ln (F_T)}{\partial r} \tag{38}$$

$$\theta_\phi = \frac{\sqrt{T_e}}{2\tan\chi}\frac{\partial \ln \phi}{\partial r} \tag{39}$$

The symbol χ represents the angle between the magnetic field lines and the wall, with $\chi = \pi/2$ indicating normal incidence with respect to the wall. In a large aspect ratio tokamak with a toroidal limiter this reduces to $\chi \approx r/(qR)$.

As a final remark on the boundary conditions, we note that the treatment carried out in Ref. [34] does not include electromagnetic effects, which are intrinsically 3-D and would require very costly full kinetic simulations to unravel. In GBS electromagnetic simulations, equation (29) is used as a boundary condition for $v_{\|e}$ and $U_{\|e}$, which gives $\psi = 0$ at the MP entrance. A detailed linear and non-linear analysis found that these boundary conditions give the same stability conditions for ideal ballooning modes as "line-tied" conditions [40].

2.4. Kinetic model for neutral atoms

We summarize the kinetic model for neutral atoms included in GBS, which is discussed in detail in [22]. A mono-atomic neutral species is considered. The kinetic treatment allows for short and long mean free path scenarios. The neutral species is subject to ionization, recombination, and charge-exchange processes. Neutral–neutral collisions, which can become important in detached scenarios, are neglected since they have a lower reaction rate than charge-exchange and ionization processes in the attached SOL regime, which is the main interest of current GBS simulations. Elastic electron–neutral collisions are neglected for the neutrals because of the small mass ratio. While molecules and their dissociation can play a role in the SOL, they are neglected here to allow us to develop a simple model to study the interaction between neutral atoms and the plasma.

The dynamics of the distribution function of a single neutral species, f_n, is described using the kinetic equation

$$\frac{\partial f_\mathrm{n}}{\partial t} + \mathbf{v}\cdot\frac{\partial f_\mathrm{n}}{\partial \mathbf{x}} = -\nu_\mathrm{iz} f_\mathrm{n} - \nu_\mathrm{cx}\left(f_\mathrm{n} - \frac{n_\mathrm{n}}{n_i} f_i\right) + \nu_\mathrm{rec} f_i. \tag{40}$$

The boundary conditions for f_n involve assuming that all impacting particles are reemitted from the wall instantly, i.e. a saturated wall. A fraction of the particles is reflected, while the rest is absorbed and released with a velocity depending on the wall properties. The distribution function of the inflowing neutrals is

$$f_\mathrm{n}(\mathbf{x}_\mathrm{b}, \mathbf{v}) = (1-\alpha_\mathrm{refl})\Gamma_\mathrm{out}(\mathbf{x}_\mathrm{b})\chi_\mathrm{in}(\mathbf{x}_\mathrm{b}, \mathbf{v}) + \alpha_\mathrm{refl}[f_\mathrm{n}(\mathbf{x}_\mathrm{b}, \mathbf{v} - 2\mathbf{v}_\mathrm{p}) + f_i(\mathbf{x}_\mathrm{b}, \mathbf{v} - 2\mathbf{v}_\mathrm{p})], \tag{41}$$

where $\mathbf{x}_\mathrm{b}$ is the position vector of a point on the limiter or divertor surface, Γ_out is the sum of ion and neutral fluxes towards the limiter or divertor plates, and $\mathbf{v}_p = v_p\hat{\mathbf{n}}$ is the perpendicular velocity with respect to the boundary. The inflowing velocity distribution χ_{in}, is set by the Knudsen cosine law

$$\chi_\mathrm{in}(\mathbf{x}_\mathrm{b}, \mathbf{v}) = \frac{3}{4\pi}\frac{m^2}{T_\mathrm{b}^2}\cos(\theta)\exp\left(-\frac{mv^2}{2T_\mathrm{b}}\right), \tag{42}$$

where $\theta = \arccos(\mathbf{v}\cdot\hat{\mathbf{n}}/v)$ and T_b is the wall temperature. The function χ_in satisfies the property $\int_{v_\mathrm{p}>0} v_\mathrm{p}\chi_\mathrm{in}\mathrm{d}v^3 = 1$. The solution of equation (40) in the adiabatic limit ($\partial_t f_\mathrm{n} \approx 0$) leads to the neutral density, parallel velocity, and temperature used in the drift reduced equations (17)–(22). The numerical treatment of the neutral particle model is outlined below in section 3.

3. Numerical implementation

GBS is aimed at global calculations of plasma turbulence within an annular domain extending over a full torus, where we must resolve both the macroscopic device scale and the ion sound Larmor gyroradius in the transport timescale. The lack of separation of amplitudes between fluctuations and background profiles, as well as the poor separation of length scales between the eddy size and the radial domain, impose a global flux-driven approach. GBS simulations involve plasma sources that build-up the profiles, which in turn drive the turbulent eddies. Hence, the interaction between the turbulent eddies and the "bulk" plasma is retained to all orders. This effect is particularly important in the study of the pressure non-linearity effect believed to saturate the turbulence [33].

The implementation of GBS can be hastily summarized as follows. A radial section of a torus, with coordinate system $(y = a\theta, x, \varphi)$ is mapped to a discrete Cartesian grid with (n_y, n_x, n_z) points for each scalar field. We denote $N = n_y \times n_x \times n_z$ as the total number of grid points. The φ coordinate is periodic, while periodicity in y can be selected for a chosen range of x – thus, we can vary between a poloidally periodic plasma, a limited plasma, or we can mix open and closed field lines. Time integration is carried out with the Runge–Kutta order 4 (RK4) algorithm.

Spatial gradients are computed using standard second order centered finite difference formulas, while the $\mathbf{E} \times \mathbf{B}$ non-linear advection terms are discretized using the Arakawa scheme [17]. The Poisson and Ampère equations can be solved using sparse matrix methods, or using a stencil-based multigrid solver, described below in section 3.3. The parallel gradient operators have been described in detail in Ref. [20]. Field-aligned and non-field-aligned strategies are possible. When the field-aligned strategy is used, the toroidal coordinate of $(U_{\parallel e}, v_{\parallel e}, \psi, v_{\parallel i})$ is displaced by half a grid point in the toroidal direction (i.e. we use staggered grids). We found that it was necessary for numerical stability to up/downwind the parallel gradients at the ends of the domain, which was also the case in TOKAM3D [12]. In effect, boundary conditions (Eqs. (28)–(34)) are implemented using forward and backward finite difference schemes to increase the numerical stability of the code.

Since the gradient operations and the time integration are both local, domain decomposition is an obvious choice for parallelization. Message passing is carried out with the MPI library, which implements communications for a distributed memory computer. We use a 3D Cartesian communicator, which in effect decomposes each scalar field in $(n_{p,x}, n_{p,y}, n_{p,z})$ subdomains residing in different processes. When sparse matrix methods for the Poisson or Ampère equations are used, collective communications are required to pass the source term into the solver. The multigrid solver, on the other hand, employs the same domain decomposition grids used for the spatial gradients.

In the following, we discuss several topics related to physical model and numerical implementation in more detail, pointing out where necessary the numerical and physical differences found with respect to the older version of GBS [14].

3.1. Manufactured solutions verification

The reliability of numerical simulation codes can only be ensured through a thorough and rigorous verification process. By a "verification process", we mean a computational procedure to ensure that the targeted physical model (here given by equations (17)–(22)) is solved correctly by the code. Traditionally, code verification has employed several approaches, the most common ones being simple physical tests (e.g., convergence towards known linear growth rates or other physical behavior) and code-to-code benchmarks. The Cyclone benchmark is a classical example illustrating these two approaches in plasma physics [52]. On the other hand, a *rigorous* code verification entails *quantifying* the discretization error and its convergence rate towards a known analytical solution.

Herein, we present a *manufactured method solution* (MMS) [53] verification of the new GBS code. MMS is a general and rigorous methodology to verify simulation codes, which was already applied to the old GBS version (cold ion model, Boussinesq approximation) by Riva et al. [54]. The principal idea behind MMS is to manufacture a solution to the model equations, and then adding analytical source terms so that the system naturally accommodates the manufactured solution. Since the analytical solution of the modified model is known, there is no conceptual difficulty in verifying the code. Simulations using the analytical source terms are carried out using progressively more refined grids, from which the discretization error and its convergence rate can be quantified.

We carry out the assessment of the correct implementation of the model equations by applying MMS as outlined in our previous publication [54]. In this manner, we ensure the correct implementation of the substantial additions to the physical model described herein. To verify the implementation of the drift-reduced Braginskii model, the manufactured solution chosen for each field reads

$$s(y, r, \varphi, t) = A_s \{B_s + C_s \sin[D_s(\varphi - qy/a)] \times \sin(E_s y + F_s) \sin[G_s x + H_s t]\}, \tag{43}$$

where A_s, B_s, C_s, D_s, E_s, F_s, G_s, and H_s are arbitrary constants and s represents the scalar fields $\{n, \Omega, v_{\parallel i}, v_{\parallel e}, T_e, T_i\}$ present in the GBS equations. The constant B_s is used to ensure $n > 0$, $T_{e,i} > 0$, while the other factors are used to calibrate the numerical error, ensuring that no term dominates the numerical error in the equations. The dependencies imposed through these constants manifest the physical problem of interest, with a term being perfectly aligned to the magnetic field lines, and a perturbation along the y-coordinate. Variation along the radius and time variation are also included.

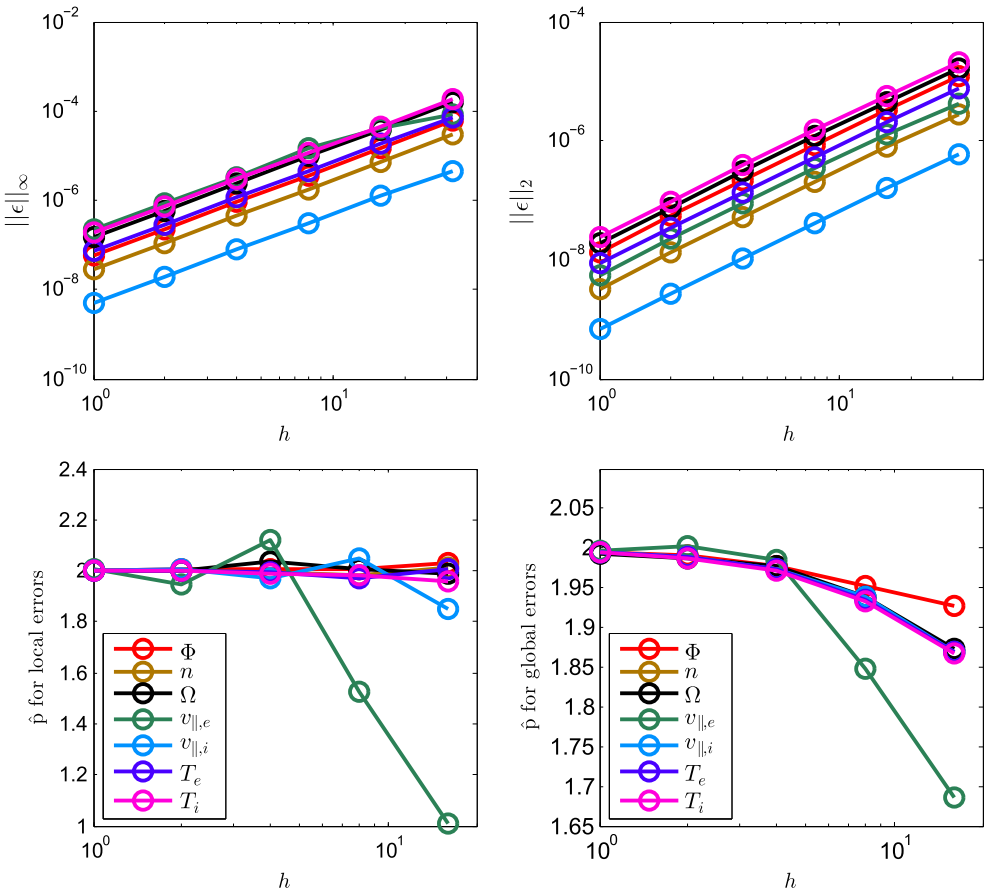

Fig. 1. $||\epsilon||_\infty$ (left) and $||\epsilon||_2$ (right) norms of the discretization error (top panels) and their respective order of accuracy estimates (bottom panels) for GBS simulations where the space/time grid is refined by a factor of 32. The refinement parameter is defined as $h = \Delta x/\Delta x_0 = \Delta y/\Delta y_0 = \Delta z/\Delta z_0 = (\Delta t/\Delta t_0)^2$.

The calculation of the source terms consists in substituting equation (43) into equations (17)–(22) for each field. This tedious process is carried out using Mathematica [55], which then also allows us to translate the analytical expressions directly to Fortran. In this manner, the possibility of introducing errors into the source terms is reduced significantly. Since the convergence of the numerical scheme used to discretize Eqs. (28)–(34) is first order, in the following we consider simple Dirichlet boundary conditions in y and x to preserve the second order convergence of the discretized interior derivatives. The solution of the full-polarization Poisson operator is verified independently in Sec. 3.3.

The quantification of the error concentrates on calculating the discretization error ϵ and the observed order of accuracy $\hat{p}$, given by

$$\epsilon = |s_h - s|\,, \tag{44}$$

$$\hat{p} = \frac{\ln\left[\left(s_{r^2h} - s_{rh}\right)/\left(s_{rh} - s_h\right)\right]}{\ln(r)}. \tag{45}$$

Here s is the analytical solution to the problem, h is a parameter representing the degree of refinement of the grid, s_h and s_{rh} represent the numerical solutions obtained using different meshes, and r represents the grid refinement factor between s_h and s_{rh}. We consider the norms $||\epsilon||_2 = \sqrt{\sum_i^N \epsilon_i^2/N}$ and $||\epsilon||_\infty = \max|\epsilon_i|$, where ϵ_i is the local numerical error at the grid point i, as means to compute the error and to calculate $\hat{p}$.

Six simulations are carried out, with mesh refinement parameters $h = 1, 2, 4, 8, 16, 32$ in each direction. The timestep is varied with $\sqrt{h}$, as the RK4 time advance is 4th order accurate compared to the 2nd order accurate spatial derivatives. The most refined grid has $(n_y, n_x, n_z) = (1024, 512, 256)$. The simulation parameters used, which need not be physical for a pure verification exercise, are $q = 2$, $\nu = 0.01$, $\rho_\star^{-1} = 100$, and $m_i/m_e = 200$. The verification results are summarized in Fig. 1, where we show the $||\epsilon||_\infty$ (left) and $||\epsilon||_2$ (right) norms of the discretization error (top), along with their order of accuracy estimates $\hat{p}$ (bottom). The discretization error, shown in logarithmic scale, decreases with slope $\hat{p} = 2$ for all the fields. Thus, it is demonstrated that equations (17)–(22) are implemented correctly in GBS, and that the chosen numerical scheme satisfies 2nd order accuracy in space and 4th order in time.

3.2. Implementation of neutral physics model

In what follows, we summarize the calculation of the neutral density, velocity, and temperature needed in equations (17)–(22). Using the method of characteristics, the formal solution to equation (40) is found. Details of the calculation are shown in Ref. [22]. The solution is then approximated in the limit where $\tau_{turb} > \tau_n$ and $\lambda_{\mathrm{mfp,n}} k_\parallel \ll 1$. Physically, this means that the neutral distribution function can be assumed to be static in the turbulent timescale (adiabatic limit), $\partial_t f_\mathrm{n} = 0$ [56], and that the mean free path of the neutrals is short compared to the parallel scalelength of the plasma structures. The latter fact is then used to decouple the perpendicular and parallel coordinates, arriving to the conclusion that each poloidal plane can be treated separately in the computation.

The formal solution to equation (40), in the adiabatic limit and assuming $\lambda_{\mathrm{mfp,n}} k_\parallel \ll 1$, becomes

$$f_\mathrm{n}(\mathbf{x}_\perp, x_\parallel, \mathbf{v}, t) = \int_0^{r_{\perp\mathrm{b}}} \left[\frac{S(\mathbf{x}'_\perp, x_\parallel, \mathbf{v}, t)}{v_\perp} + \delta(r'_\perp - r_{\perp\mathrm{b}}) f_\mathrm{n}(\mathbf{x}'_{\perp b}, x_\parallel, \mathbf{v}, t) \right] \times \exp\left[-\frac{1}{v_\perp} \int_0^{r'_\perp} \nu_\mathrm{eff}(\mathbf{x}''_\perp, x_\parallel, t) \mathrm{d}r''_\perp \right] \mathrm{d}r'_\perp, \tag{46}$$

where $r'_\perp$ is defined in the expression $\mathbf{x}'_\perp = \mathbf{x} - r'_\perp \mathbf{v}_\perp / v_\perp$, $r_{\perp\mathrm{b}}$ indicates the distance of $\mathbf{x}$ to the wall along the $\mathbf{v}$ direction, and $\mathbf{v}_\perp$ is the perpendicular velocity. The effective cross-section for removal of the neutrals particles is given by $\nu_\mathrm{eff} = \nu_\mathrm{iz} + \nu_\mathrm{cx}$. Here the single prime notation indicates the source location of neutral particles, while the double primes indicate locations along a path integral between x' (source) and x (target). Hereafter, since we have expressed the solution in a steady-state form, and where the poloidal planes are decoupled, we drop the $x_\parallel$ and t labels to simplify the notation.

Equation (46) involves a volumetric neutral source term resulting from charge-exchange and recombination processes, given by

$$S(\mathbf{x}'_\perp, \mathbf{v}) = \nu_\mathrm{cx}(\mathbf{x}'_\perp) n_\mathrm{n}(\mathbf{x}'_\perp) \Phi_\mathrm{i}(\mathbf{x}'_\perp, \mathbf{v}) + \nu_\mathrm{rec}(\mathbf{x}'_\perp) f_\mathrm{i}(\mathbf{x}'_\perp, \mathbf{v}), \tag{47}$$

where Φ_i is the velocity distribution for the ions, and the source term from the wall, $\delta(r' - r'_\mathrm{b}) f_\mathrm{n}(\mathbf{x}'_\mathrm{b}, \mathbf{v})$, given by the boundary conditions (equation (41)).

The recombination term in equation (46), together with the ion recycling term $\Gamma_{\mathrm{out},i}$ arising from the boundary conditions, do not depend on the neutral distribution function and can be evaluated using the bulk plasma quantities. On the other hand, the charge-exchange and the reflected and re-emitted neutrals depend on $n_\mathrm{n}(\mathbf{x}_\perp)$, which must be computed.

A linear integral equation for $n_\mathrm{n}(\mathbf{x}_\perp)$ is obtained by integrating equation (46) in velocity space. After extensive rearrangement (see [22]), the following expression is obtained:

$$n_\mathrm{n}(\mathbf{x}_\perp) = \int_D n_\mathrm{n}(\mathbf{x}'_\perp) \nu_\mathrm{cx}(\mathbf{x}'_\perp) K_{\mathrm{p}\to\mathrm{p}}(\mathbf{x}_\perp, \mathbf{x}'_\perp) \mathrm{d}A' + \int_{\partial D} \Gamma_\mathrm{out}(\mathbf{x}'_{\perp\mathrm{b}}) K_{\mathrm{b}\to\mathrm{p}}(\mathbf{x}_\perp, \mathbf{x}'_{\perp\mathrm{b}}) \mathrm{d}a'_\mathrm{b} + n_{\mathrm{n,rec}}(\mathbf{x}_\perp), \tag{48}$$

where $\mathrm{d}A'$ is an infinitesimal area in the perpendicular plane D, while $\mathrm{d}a'_\mathrm{b}$ represents an infinitesimal distance along the boundary ∂D. The perpendicular component of neutral and ion flux outflowing into the boundary, Γ_out, can be obtained from the solution of

$$\Gamma_\mathrm{out}(\mathbf{x}_{\perp\mathrm{b}}) = \int v_\perp \cos\theta f_\mathrm{n}(\mathbf{x}_{\perp\mathrm{b}}, \mathbf{v}_\perp) \mathrm{d}\mathbf{v}_\perp + \Gamma_{\mathrm{out,i}}(\mathbf{x}_{\perp\mathrm{b}}) \tag{49}$$

and where $\theta = \arccos|\mathbf{v}_\perp \cdot \hat{\mathbf{n}} / v_\perp|$ is the angle between $\mathbf{v}_\perp / v_\perp$ and $\hat{\mathbf{n}}$ at the target location, $\mathbf{x}_{\perp\mathrm{b}}$. The following kernel functions, involving integrals in velocity space, are defined

$$K_{\mathrm{p}\to\mathrm{p}}(\mathbf{x}_\perp, \mathbf{x}'_\perp) = \int_0^\infty \frac{1}{r'_\perp} \Phi_{\perp\mathrm{i}}(\mathbf{x}'_\perp, \mathbf{v}_\perp) \exp\left[-\frac{1}{v_\perp} \int_0^{r'_\perp} \nu_\mathrm{eff}(\mathbf{x}''_\perp) \mathrm{d}r''_\perp \right] \mathrm{d}v_\perp \tag{50}$$

$$K_{\mathrm{b}\to\mathrm{p}}(\mathbf{x}_\perp, \mathbf{x}'_{\perp\mathrm{b}}) = \int_0^\infty \frac{v_\perp}{r'_\perp} \cos\theta' \chi_{\perp\mathrm{in}}(\mathbf{x}'_{\perp\mathrm{b}}, \mathbf{v}_\perp) \exp\left[-\frac{1}{v_\perp} \int_0^{r'_\perp} \nu_\mathrm{eff}(\mathbf{x}''_\perp) \mathrm{d}r''_\perp \right] \mathrm{d}v_\perp \tag{51}$$

$$K_{\mathrm{p}\to\mathrm{b}}(\mathbf{x}_{\perp\mathrm{b}}, \mathbf{x}'_\perp) = \int_0^\infty \frac{v_\perp}{r'_\perp} \cos\theta \Phi_{\perp\mathrm{i}}(\mathbf{x}'_\perp, \mathbf{v}_\perp) \exp\left[-\frac{1}{v_\perp} \int_0^{r'_\perp} \nu_\mathrm{eff}(\mathbf{x}''_\perp) \mathrm{d}r''_\perp \right] \mathrm{d}v_\perp \tag{52}$$

$$K_{\mathrm{b}\to\mathrm{b}}(\mathbf{x}_{\perp\mathrm{b}},\mathbf{x}'_{\perp\mathrm{b}}) = \int_0^\infty \frac{v_\perp^2}{r'_\perp}\cos\theta\cos\theta'\,\chi_{\perp\mathrm{in}}(\mathbf{x}'_{\mathrm{b}},\mathbf{v})\exp\left[-\frac{1}{v_\perp}\int_0^{r'_\perp}\nu_{\mathrm{eff}}(\mathbf{x}''_\perp)\mathrm{d}r''_\perp\right]\mathrm{d}v_\perp, \tag{53}$$

where $\Phi_{\perp\mathrm{i}}(\mathbf{x}_\perp,\mathbf{v}_\perp)=\int\Phi_{\mathrm{i}}(\mathbf{x}_\perp,\mathbf{v})\mathrm{d}v_\parallel$ and $\chi_{\perp\mathrm{in}}(\mathbf{x}_\perp,\mathbf{v}_\perp)=\int\chi_{\mathrm{in}}(\mathbf{x}_\perp,\mathbf{v})\mathrm{d}v_\parallel$.

These kernels are interpreted as the neutral particles originating/arriving from/to the plasma or the boundary. The exponentially decaying factors take into account neutral losses due to ionization and charge-exchange collisions along the particle trajectory. They do not depend on f_{n} or any of its moments, and they can be evaluated from the bulk plasma moments. Hence, equations (46) and (49) can now be discretized, and assume the matrix form

$$\begin{bmatrix} n_{\mathrm{n}} \\ \Gamma_{\mathrm{out}} \end{bmatrix} = \begin{bmatrix} K_{\mathrm{p}\to\mathrm{p}} & K_{\mathrm{b}\to\mathrm{p}} \\ K_{\mathrm{p}\to\mathrm{b}} & K_{\mathrm{b}\to\mathrm{b}} \end{bmatrix}\cdot\begin{bmatrix} n_{\mathrm{n}} \\ \Gamma_{\mathrm{out}} \end{bmatrix} + \begin{bmatrix} n_{\mathrm{n,rec}} \\ \Gamma_{\mathrm{out,rec}}+\Gamma_{\mathrm{out,i}} \end{bmatrix}. \tag{54}$$

This linear system is dense, with about a third of the matrix elements filled, typically. The fraction of non-zero entries decreases with the plasma size. In GBS, equation (54) is solved using standard dense matrix solvers. Once the neutral density is known, the entire distribution function is readily obtained from equation (46), which allows to compute the rest of the fluid moments such as $v_{\parallel\mathrm{n}}$ and T_{n}.

Since the solution of equation (54) is rather costly, the neutral density is recalculated on a timescale longer than the timestep associated with the ion and electron fluid equations. On the other hand, the interaction terms in the plasma equations, such as the ionization source and the neutral collision cross sections, which depend also on the temperature and other plasma quantities, are updated every time step. Finally, we remark that several convergence tests ensuring sufficient precision of the solution are performed in [22].

3.3. Implementation and verification of a multigrid solver for the Poisson and Ampère equations

Multigrid methods are powerful computational algorithms based on hierarchical discretizations [57,58]. The fundamental idea of multigrid methods is to accelerate the convergence of classical iterative methods, such as the Jacobi and Gauss–Seidel iterations, by solving progressively coarser problems where low wavenumber error in the solution vector can be removed efficiently.

Geometric multigrid, which can be written in terms of simple stencil operations, can be a $\mathcal{O}(N)$ method when properly designed. Additionally, since the operators map to local grid operations, it can be parallelized using standard domain decomposition techniques. For this reason, we find multigrid methods to be an ideal match to solve the generalized Poisson and Ampère equations ((25) and (26)) in GBS. We have developed a Fortran 2008, object based 2-D multigrid solver employing the standard stencil-based approach described in [57,58].

The solver can compute a solution for model equations of the form

$$\nabla\cdot(\nabla_\perp\xi(y,x)) - \lambda(y,x)\xi(y,x) = S_\xi(y,x) \tag{55}$$

$$\nabla\cdot(\lambda(y,x)\nabla_\perp\xi(y,x)) = S_\xi(y,x), \tag{56}$$

which can be used to express the Poisson equation with or without the Boussinesq approximation and the generalized Ampère operator. In these model problems, ξ represents the scalar potential function to obtain, λ is a known scalar field (e.g. the plasma density), S_ξ is a source term (e.g. the charge or the current).

The differential operators have been implemented using a finite volume approach, as suggested in [58] for variable coefficient problems. In GBS, in addition to the scalar λ inside the operator, one must also treat the shaping coefficients [20]. We express the problem in weak form, and the differential operator is treated using the divergence theorem $\int\nabla\cdot(\lambda\nabla_\perp\xi)\,\mathrm{d}V = \int\lambda\left(\nabla_\perp\xi\cdot\hat{\mathbf{n}}\right)\mathrm{d}\ell$, which gives a line integral ($\hat{\mathbf{n}}$ is an outward pointing vector normal to the integration contour, see Fig. 2). In stencil notation, the 2nd order accurate differential operator is

$$\mathbf{D}_{(y,x)} = \begin{pmatrix} \delta_{(+1,-1)} & \delta_{(+1,+0)} & \delta_{(+1,+1)} \\ \delta_{(+0,-1)} & \delta_{(+0,+0)} & \delta_{(+0,+1)} \\ \delta_{(-1,-1)} & \delta_{(-1,+0)} & \delta_{(-1,+1)} \end{pmatrix},$$

$$\delta_{(+0,+0)} = -\left\{\frac{1}{2\Delta y^2}\left[\left(\lambda g_{yy}\right)_{(-1,+0)} + 2\left(\lambda g_{yy}\right)_{(+0,+0)} + \left(\lambda g_{yy}\right)_{(+1,+0)}\right]\right.$$
$$\left. + \frac{1}{2\Delta x^2}\left[\left(\lambda g_{xx}\right)_{(+0,-1)} + 2\left(\lambda g_{xx}\right)_{(+0,+0)} + \left(\lambda g_{xx}\right)_{(+0,+1)}\right]\right\}$$

$$\delta_{(-1,+0)} = \frac{1}{2\Delta y^2}\left[\left(\lambda g_{yy}\right)_{(-1,+0)} + \left(\lambda g_{yy}\right)_{(0,0)}\right] - \frac{1}{8\Delta x\Delta y}\left[\left(\lambda g_{xy}\right)_{(+0,+1)} - \left(\lambda g_{xy}\right)_{(+0,-1)}\right]$$

$$\delta_{(+1,+0)} = \frac{1}{2\Delta y^2}\left[\left(\lambda g_{yy}\right)_{(+1,+0)} + \left(\lambda g_{yy}\right)_{(0,0)}\right] - \frac{1}{8\Delta x\Delta y}\left[\left(\lambda g_{xy}\right)_{(+0,-1)} - \left(\lambda g_{xy}\right)_{(+0,+1)}\right]$$

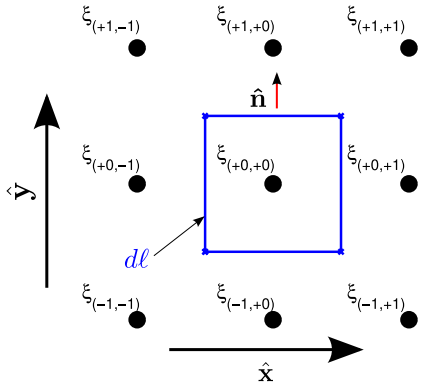

Fig. 2. Potential function χ mapped to a 2D Cartesian grid, showing the location of the grid indices, together with the integration contour (blue line). The vector $\hat{\mathbf{n}}$ (red arrow) points outwards from each side of the square integration contour. (For interpretation of the references to color in this figure legend, the reader is referred to the web version of this article.)

$$\delta_{(+0,-1)} = \frac{1}{2\Delta x^2}\left[(\lambda g_{xx})_{(+0,-1)} + (\lambda g_{xx})_{(0,0)}\right] - \frac{1}{8\Delta x\Delta y}\left[\left(\lambda g_{xy}\right)_{(-1,+0)} - \left(\lambda g_{xy}\right)_{(+1,+0)}\right]$$

$$\delta_{(+0,+1)} = \frac{1}{2\Delta x^2}\left[(\lambda g_{xx})_{(+0,+1)} + (\lambda g_{xx})_{(0,0)}\right] - \frac{1}{8\Delta x\Delta y}\left[\left(\lambda g_{xy}\right)_{(+1,+0)} - \left(\lambda g_{xy}\right)_{(-1,+0)}\right]$$

$$\delta_{(-1,+1)} = -\frac{1}{8\Delta x\Delta y}\left[\left(\lambda g_{xy}\right)_{(-1,+0)} + 2\left(\lambda g_{xy}\right)_{(+0,+0)} + \left(\lambda g_{xy}\right)_{(+0,+1)}\right]$$

$$\delta_{(+1,-1)} = -\frac{1}{8\Delta x\Delta y}\left[\left(\lambda g_{xy}\right)_{(+1,+0)} + 2\left(\lambda g_{xy}\right)_{(+0,+0)} + \left(\lambda g_{xy}\right)_{(+0,-1)}\right]$$

$$\delta_{(+1,+1)} = +\frac{1}{8\Delta x\Delta y}\left[\left(\lambda g_{xy}\right)_{(+0,+1)} + 2\left(\lambda g_{xy}\right)_{(+0,+0)} + \left(\lambda g_{xy}\right)_{(+1,+0)}\right]$$

$$\delta_{(-1,-1)} = +\frac{1}{8\Delta x\Delta y}\left[\left(\lambda g_{xy}\right)_{(+0,-1)} + 2\left(\lambda g_{xy}\right)_{(+0,+0)} + \left(\lambda g_{xy}\right)_{(-1,+0)}\right].$$

Here, the subscripts indicates, in a 2-D Cartesian grid, the indices where the quantities are defined. Where the integration requires values at the half indices $(\pm 1/2, \pm 1/2)$, the quantities are obtained using linear interpolation. In addition to the scalar function λ, the metric coefficients g_{ij} enter the computation. The discretization procedure ensures self-adjointness of the operator and, furthermore, takes into account the variation of the metric coefficients automatically.

The grid transfer operations implemented, e.g. *restriction* and *prolongation*, are the full weighting scheme and the linear interpolation operators

$$\mathbf{R}_i = \frac{1}{16}\begin{pmatrix} 1 & 2 & 1 \\ 2 & 4 & 2 \\ 1 & 2 & 1 \end{pmatrix}, \qquad \mathbf{I}_{i,x} = \frac{1}{2}\begin{pmatrix} 1 & 1 \end{pmatrix}, \qquad \mathbf{I}_{i,y} = \frac{1}{2}\begin{pmatrix} 1 \\ 1 \end{pmatrix}.$$

The operators are all modified at the boundary, following the method outlined by [58]. The relaxation methods implemented are the relaxed Jacobi, Successive Over Relaxation, and Red–Black Gauss–Seidel iterations. Non-homogeneous Dirichlet and Von Neumann boundary conditions can be specified, with the condition that at least one of the boundaries of the domain must fulfill a Dirichlet condition. We have verified the 2nd order accuracy of this solver in the context of a stand-alone program with a simple analytic solution (a product of harmonic functions). As an example, in Fig. 3 we show the convergence test carried out for the non-Boussinesq Poisson equation with solution $\xi_{\text{th}}(y,x) = \sin(k_y y)\sin(k_x x)$, using spatially varying coefficients mimicking

$$\lambda = \lambda_0\left[1 + sin^2\left(\frac{2\pi k_p y}{L_y}\right)\exp\left(\frac{(x-x_0)^2}{2\sigma^2}\right)\right]. \tag{57}$$

In Fig. 3 we demonstrate (a) 2nd order accuracy of the solver and (b) good convergence properties even when the wavenumbers of $\lambda(y,x)$, k_p and σ, are large.

Verifying the non-linear steady state is a different matter. The chaotic nature of the system amplifies tiny numerical differences over time, leading to different plasma states. For this reason, we carry out two identical simulations that use two Poisson different solvers (multigrid vs. PMUMPS [59,60], a parallel sparse solver), and we compare the mean profiles and the turbulence. Fig. 4 shows such comparison, in particular (a) for the relative amplitude vs. poloidal wavenumber $k_\theta \rho_{s0}$ and (b) for the probability distribution function (PDF) of the potential fluctuations. Here we note that the moments

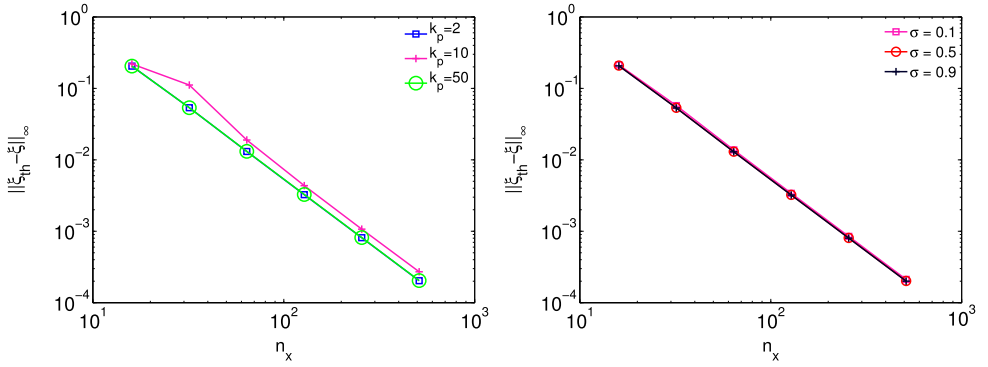

Fig. 3. Infinity norm of the numerical error, $||\xi_{th} - \xi||_\infty$, found in multigrid solution of equation (56) using equation (57) as a spatially varying coefficient with wavenumbers k_p (left) and σ (right). We use $k_x = k_y = 4$, $n_y = 4n_x$, $L_y = 800$, and Dirichlet boundary conditions on all four sides.

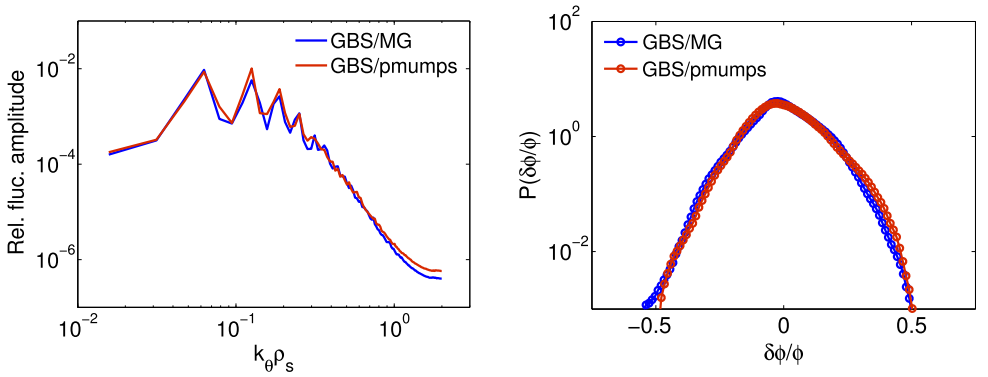

Fig. 4. Relative fluctuation amplitude vs. poloidal wavenumber (left) and probability distribution function of the density fluctuations (right), for identical GBS simulations carried out using a multigrid or a sparse matrix solver. GBS simulation parameters were $L_x = 100$, $L_y = 400$, $\rho_\star^{-1} = 250$, $\nu = 0.1$, $\beta_{e0} = 0$.

of the PDF are subject to time averaging error due to finite sampling. In spite of this, the moments of the PDF (mean, root-mean-square, and skewness) match each other quite well. The steady-state plasma profiles are also a good match.

Convergence for the problems of interest is very fast, with the norm of the relative error dropping below 10^{-10} in 3 or 4 multigrid iterations (V(3, 3)-cycles) with 6 grid levels in GBS simulations. Fastest convergence and robustness is found using an overrelaxed Red–Black Gauss–Seidel method (relaxation constant $\omega \approx 1.2$), which can improve convergence when grid anisotropy and variable coefficients are present. The metric coefficients used in GBS, as an example, the $\hat{s} - \alpha$ model, involve a severely deformed metric that slows down convergence. In effect, as one of the metric coefficients increases like $g_{yy} \propto (\hat{s}\theta)^2$, convergence must be improved by further increasing the relaxation constant. Even with a large relaxation parameter, the cross derivative terms $\sim \hat{s}\theta\partial_{xy}$ remain troublesome. Overall, the convergence properties of the solver remain appropriate for $\hat{s} \approx 1$. With this setup, the GBS multigrid solver is faster than the backsolve step of standard sparse linear solvers.

The largest gains when integrating a multigrid solver into GBS stem from improved parallelism, in particular, in the strong scaling, and from the possibility of defining time varying operators. Even for the simple case where the Boussinesq operator $\nabla_\perp^2\phi$ is used, the parallel sparse solver scales poorly and became a bottleneck towards large size simulations. As an example of such a case, in Fig. 5 we show the strong and weak scalings and timings for GBS using parallel multigrid or PMUMPS. The test was carried out at Helios, a BullX B510 supercomputer based on Intel Xeon processors operated by the International Fusion Energy Research Centre. In the strong scaling, the simulations have a grid size $(n_y, n_x) = (2048, 256)$, which corresponds to plasmas even larger than the ones discussed in [44]. The poloidal grid size is maintained constant while the number of cores in each poloidal plane is increased. This approach involves a direct test on the scalability of the Poisson solver itself.

Using multigrid represents a tremendous advantage with respect to the PMUMPS simulations, with a factor of 5 gain in speed at 32 cores per poloidal plane. For the multigrid runs we observe a superlinear speed-up when going from 16 to 32 cores per poloidal plane. This is due to reduced memory usage in each core, which then leads to better cache use and improves the solver's performance. On the left-bottom panel of Fig. 5, note that the multigrid solver takes a small fraction of the total timestep. On the other hand, when using PMUMPS the computational effort is completely dominated by the backsolve of the Poisson operator. Other parallel sparse solvers, such as PARDISO [61], display similar performance as PMUMPS.

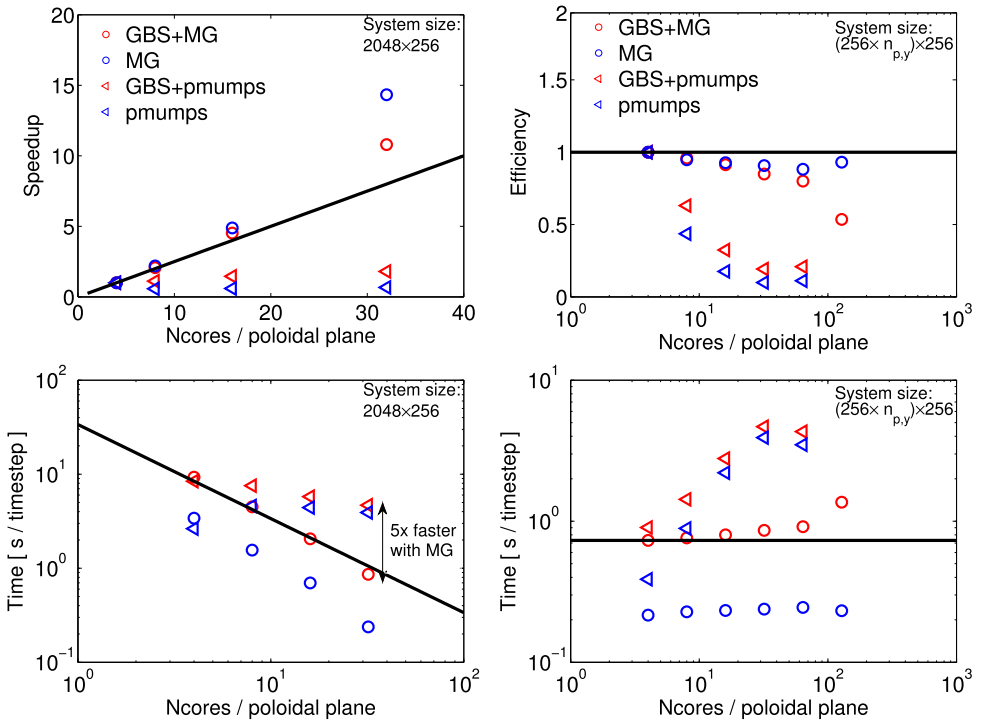

Fig. 5. Strong (left) and weak (right) scalings (top) and timings (bottom) are shown for GBS simulations using either parallel multigrid or parallel MUMPS. (left, constant grid size with increasing number of cores) (right, increasing grid size with constant number of points per core). In the strong scaling we take a fixed grid size and increase the number of cores per poloidal plane from 4 to 32. In the weak scaling, the problem size and the number of cores in the y direction, Ncy, are both increased by a factor of 8. The test was carried out at Helios, a BullX B510 supercomputer based on Intel Xeon processors operated by the International Fusion Energy Research Centre.

For the weak scaling and timing (right top and bottom panels of Fig. 5), we choose a fixed number of points per core, and then increase the problem size and the number of cores at the same rate. This exercise tests whether a code can treat increasingly larger problems in an efficient manner. As we observe in the figure, the new version of GBS, with its multigrid solver, is capable of treating large grid sizes just as efficiently as it can deal with small ones. Finally, we note that the multigrid solver solution time in GBS scales as $\mathcal{O}(N)$, as shown by the constant time to solution on the bottom-right panel of Fig. 5.

In Ref. [14], a time varying operator was implemented for the Ampère problem (equation (26)) using standard sparse methods. The operator had to be periodically rebuilt and diagonalized. For speed considerations, this process took place every 10 timesteps, and the LU decomposed operator was used to obtain $v_{\|e}$ and ψ every timestep (more specifically, every Runge–Kutta substep). Furthermore, the number of cores remained bounded by the number of poloidal planes, mainly because of memory constraints. In the new version of GBS, we find that the Ampère equation can be solved with the same efficiency and scalability shown for the Poisson problem. Hence, we can include electromagnetic effects with only a 10% penalty in speed respect to the electrostatic case, and solving the time dependent operator.

4. Physical applications

As a showcase of the new capabilities of GBS, we present two modeling applications using the simple field-aligned grid with flat q. First, we demonstrate the propagation of coherent plasma filaments (blobs) in a geometry corresponding to that of the TORPEX Simple Magnetized Torus (SMT) [15]. We use this simple example, in particular, to demonstrate the effects of finite ion temperature and the full-polarization terms in the vorticity equation. Then, we show a more complex simulation of the full turbulent dynamics in a tokamak SOL.

4.1. Seeded blob simulations

GBS is used here to simulate blob dynamics in the SMT geometry, in particular, TORPEX [15]. This machine is characterized by helical field lines terminating on the vessel walls, resulting from the superposition of toroidal (B_φ) and vertical (B_y) magnetic fields. The main device parameters are $R = 1$ m, $a = 0.2$ m, $B_\varphi = 75$ mT, $B_y \sim 2$ mT. The number of field line turns around the torus, N_φ, can be varied between 2 and 16. Thus, the main elements of scrape-off layer turbulence (curvature driven modes, helical field lines, and sheath physics) are present, although in a simplified setting with excellent diagnostic coverage.

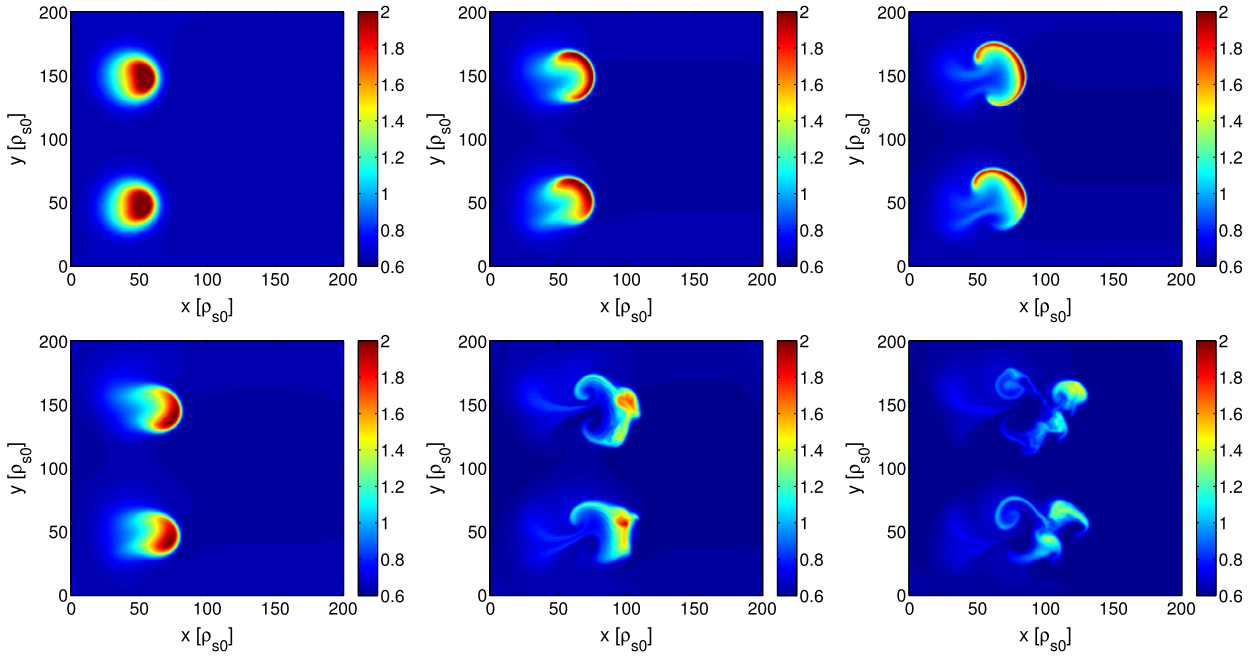

Fig. 6. Plasma density snapshots at $t = 0.16, 0.32, 0.48 R/c_{s0}$ (left, center, right) in seeded blob simulations using TORPEX geometry and parameters. The top row shows the blob propagation in a cold-ion, Boussinesq model, while the bottom row, including T_i effects and non-Boussinesq terms shows significantly faster propagation.

In what follows, we consider *seeded* blob simulations, where we follow the dynamics of a single blob used as an initial condition for the simulation. The setup is identical to previous blob simulations carried out with GBS [31], but we include T_i physics ($\tau = 2$) and the full-polarization terms. The following parameters are used: $\rho_\star^{-1} = 500$, $L_y = L_x = 200$, $N_\varphi = 2$, $\nu = 0.1$, which correspond to $n_{e0} = 10^{17}$ m^{-3} and $T_{e0} = 1$ eV. Electromagnetic terms are neglected due to the small β. The grid resolution is $(n_y, n_x, n_z) = (256, 256, 64)$, and we consider the following blob sizes $a_\perp = \{0.5, 1.0, 2.0\} a_0$, where $a_0 = \left[4(2\pi N_\varphi)^2 \rho_\star^{-1}\right]^{1/5} \approx 13\rho_{s0}$ is the blob reference size. The initial longitudinal (e.g. along the field line) blob size considered is $a_\parallel = 2\pi N_\varphi$, which corresponds to a connected blob.

The simulation is initialized using a field-line-following Gaussian perturbation in n, T_e, and T_i. The electrostatic potential starts as a small dipole "seed" to initialize the motion, and we require a balance between the leading order terms in the Ohm's law. The blob is propelled by an $\mathbf{E} \times \mathbf{B}$ flow resulting from the dipole structure of the electric field, which is driven by the magnetic field curvature terms. As the blob accelerates it deforms into a mushroom shaped structure, and then turbulent features form, leading to loss of coherence. The blob break-up takes place after it travels a significant fraction of the radial extension of the vessel.

Fig. 6 shows an example of such process, comparing our previous Boussinesq simulations with $\tau = 0$ to the $\tau = 2$, non-Boussinesq case. The time evolution of the plasma density is shown for $a_\perp = 1 a_0$. Similar dynamics is observed for the other blob sizes. Each column shows a density snapshot in time, with $t = 0.16, 0.32, 0.48 R/c_{s0}$. The time scale of the physical processes (acceleration, propagation, break-up) is significantly faster in simulations with $\tau = 2$. This result is qualitatively consistent with recent blob simulations using fluid and gyrofluid codes [62,7,63,64], in the sense that non-Boussinesq blobs with finite T_i dynamics propagate faster than their cold ion counterparts and can have enhanced coherence. An exhaustive benchmark and validation exercise for seeded blob motion in TORPEX, including GBS and other codes, has been carried out in the cold ion limit [65], and a similar exercise is taking place using data from the MAST tokamak [66].

4.2. Scrape-off layer simulation including a closed field line region

In the past, GBS simulations focused on the plasma dynamics of a SOL region with only open magnetic field lines. However, recent infrared thermography measurements have shown very steep plasma profiles just outside the LCFS [67]. Steep plasma profiles are typically associated to radially sheared electric fields, for instance, as in the high confinement mode (H-mode) transport barrier. This type of phenomena, which must forcibly include interaction between the open and closed magnetic field line regions, strongly motivated the inclusion of a confined region in GBS to fuel the SOL more realistically than in our previous work. Herein we present the first such simulations.

Results of a GBS SOL simulation including a closed field line region are shown in Fig. 7. The parameters are $L_y = 1600$, $L_x = 100$, $\rho_\star^{-1} = 1000$, $\nu = 0.01$, $q = 4$ (flat profile), $\beta_{e0} = 0$, with resolution $(n_y, n_x, n_z) = (1024, 64, 128)$. The source terms are poloidally and toroidally uniform, with the radial profile $S = 0.25 \exp\left(-(x/5)^2\right)$. The sources are centered around the

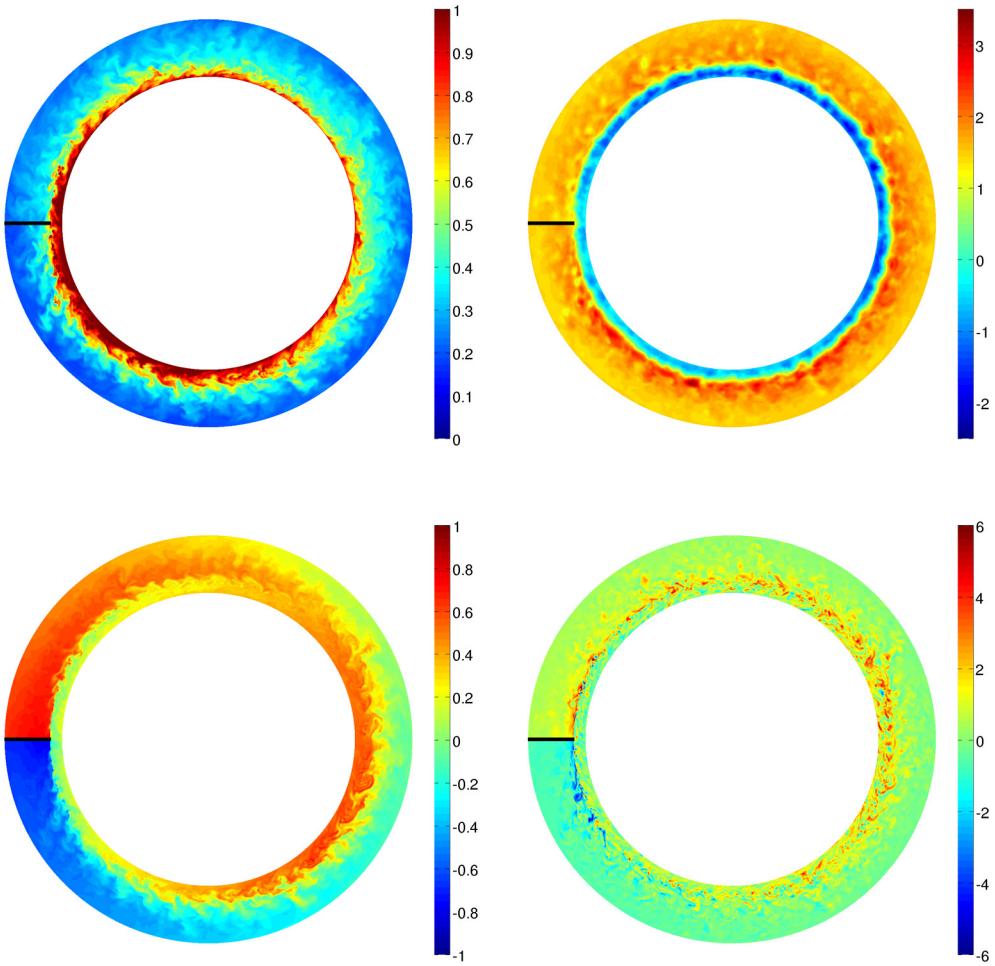

Fig. 7. Poloidal cross sections of density (top left), electrostatic potential (top right), ion parallel velocity (bottom left) and electron parallel velocity (bottom right) in GBS simulations coupling the plasma edge with the scrape-off layer. The limiter is an infinitely thin wedge shown as a thick black line in the SOL region.

inner boundary of the simulation domain. An equivalent simulation, albeit without the confined region, is described in [42]. As a first approach to studying a complex physical system, we use a Boussinesq model with cold ions. The plasma flux surface geometry is circular, with an infinitely-thin wedge limiter placed at the high-field-side, mimicking an inner-wall-limited plasma. Similar configurations have been considered by other codes [10,68].

The plasma dynamics found differs from previous GBS results in significant ways. To begin, there is a strong interplay between sheath-driven flows and the confined region. A strong inwards radial $v_{\|i}$ flux from the SOL drives intrinsic rotation in the plasma edge region. The parallel flows, in fact, do not equalize along the field line (bottom left of Fig. 7), which in turn drives a poloidal asymmetry in the density due to parallel momentum balance (top left of Fig. 7). A similar effect was found by Tamain et al. [68], although in their case the density strongly ballooned in the low-field-side, and the flow asymmetry was poloidally mirrored with respect to ours.

Some other interesting phenomena appear in the simulation. The electrostatic potential changes sign around the LCFS, and the sheath cannot sustain the typical potential of $\phi \sim 3T_e$ due to the presence of field aligned currents at the sheath (see, for example, [37]). This effect creates a large floating potential in the near SOL, which in turn drives a strong $v_{\|e}$ feature close to the limiters. In addition, a strong electric field gradient is found around the LCFS, with the flow being clockwise in the confined region and counter-clockwise in the SOL. This is exactly the simulation scenario where effects such as blob creation and turbulence suppression arise and can be studied in a natural and self-consistent way.

5. Summary and conclusions

The present paper describes a new version of GBS, a 3D two-fluid global, flux-driven plasma turbulence code to simulate the turbulent dynamics at the boundary of tokamaks. The development of the new GBS version was in part driven by the objective of studying SOL turbulent dynamics in medium size tokamaks and beyond with a reliable model. We remark two

aspects of the present work, which are intertwined: model extensions increasing the physics fidelity of the simulations, and the computational improvements allowing them.

The model extensions include neutral atom physics, finite ion temperature, and a more sophisticated treatment of the polarization drift. The neutral atom model treats a single, monoatomic kinetic species subject to ionization, charge exchange, and recombination processes. The effect of these processes is included in the plasma fluid equations through a Braginskii-like closure that adds particle, momentum, and heat sinks and sources related to the neutrals. GBS implements, in fact, drift-reduced equations for ion and electron density, momentum, and temperature, with a charge conservation (vorticity) equation. The latter includes a more refined description of the polarization drift, retaining a non-linear coupling between density and electrostatic potential.

Concurrently with these model improvements, the GBS code has been completely refactored, for instance, by introducing a 3-D Cartesian communicator and a scalable parallel multigrid solver. Thanks to these improvements, we report enhanced parallel scalability, with the possibility of treating electromagnetic fluctuations at any plasma size very efficiently. The introduction of multigrid techniques was also paramount for eliminating the Boussinesq approximation. The implementation of the model equations is verified using the MMS method, demonstrating that the discretization of the fluid model equations attains the desired accuracy order. This process gives us full confidence in the reliability and fidelity of the code. Indeed, simple physics examples obtained using the new GBS code already point towards new an exciting directions, such as the simulations concurrently including closed and open field line regions.

Acknowledgements

Part of the simulations presented herein were carried out using the HELIOS supercomputer system at Computational Simulation Centre of International Fusion Energy Research Centre (IFERC-CSC), Aomori, Japan, under the Broader Approach collaboration between Euratom and Japan, implemented by Fusion for Energy and JAEA; and part were carried out at the Swiss National Supercomputing Centre (CSCS) under Project IDs s544 and s549. This research was supported in part by the Swiss National Science Foundation, and has been carried out within the framework of the EUROfusion Consortium and has received funding from the Euratom research and training programme 2014–2018 under grant agreement No. 633053. The views and opinions expressed herein do not necessarily reflect those of the European Commission.

Appendix A. Expressions for the polarization drift

The derivation of the polarization drift and its divergence begins with the Braginskii equation for the αth component of the momentum of the ion species, written in physical units:

$$\frac{\partial}{\partial t}\left(m_i n_i v_{i\alpha}\right) + \frac{\partial}{\partial x_\beta}\left(m_i n_i \left\langle V_{i\alpha} V_{i\beta}\right\rangle\right) - Z_i e n_i \left[E_\alpha + (\mathbf{v}_i \times \mathbf{B})_\alpha\right] = R_\alpha \,, \tag{A.1}$$

where R_α is the momentum exchange between species, $\langle\rangle$ implies averaging over the distribution function, and Einstein summation notation is used. The velocity is split between mean and random components, $\mathbf{V}_i = \mathbf{v}_i' + \mathbf{v}_i$, with $\langle \mathbf{v}_i' \rangle = 0$, which allows us to write

$$\begin{aligned}\frac{\partial}{\partial x_\beta}\left(m_i n_i \left\langle V_{i\alpha} V_{i\beta}\right\rangle\right) &= \frac{\partial}{\partial x_\beta}\left(m_i n_i v_{i\alpha} v_{i\beta}\right) + \frac{\partial}{\partial x_\beta}\left(m_i n_i \left\langle v_{i\alpha} v_{i\beta}\right\rangle\right) \\ &= \mathbf{v}_i \cdot \nabla\left(m_i n_i \mathbf{v}_i\right) + m_i n_i \mathbf{v}_i \nabla\cdot\mathbf{v}_i + \nabla p_i + \nabla\cdot\Pi_i .\end{aligned} \tag{A.2}$$

In the expression above, the scalar pressure and the ion stress tensor take their usual forms, and we use the product rule to expand the term involving the mean velocity.

The drift reduction follows as usual. The procedure employed is general, but we restrict the analysis to the case of a large aspect ratio tokamak, which allows us to simplify the polarization velocity and its divergence considerably. Taking the cross product of equation (A.1) with $\hat{\mathbf{b}}_0$, having approximated $\mathbf{B}$ with its equilibrium value, yields

$$\begin{aligned}\mathbf{v}_{\perp i} = &\frac{\hat{\mathbf{b}}_0 \times \nabla_\perp \phi}{B} + \frac{\hat{\mathbf{b}}_0 \times \nabla p_i}{Z_i e n_i B} + \frac{\hat{\mathbf{b}}_0 \times \nabla\cdot\Pi_i}{Z_i e n_i B} + \\ &\frac{\hat{\mathbf{b}}_0}{Z_i e n_i B} \times \frac{\mathrm{d}}{\mathrm{d}t}(m_i n_i \mathbf{v}_i) + \frac{\hat{\mathbf{b}}_0 \times m \mathbf{v}_i \nabla\cdot\mathbf{v}_i}{Z_i e B}.\end{aligned} \tag{A.3}$$

The first two terms are identified as the $\mathbf{E}\times\mathbf{B}$ and diamagnetic drifts, and together with $v_{\parallel i}$ represent in fact the 0th order solution of equation (A.1)

$$\mathbf{v}_{0i} = v_{\parallel i}\hat{\mathbf{b}} + \mathbf{v}_{\mathbf{E}\times\mathbf{B}} + \mathbf{v}_{\star i} \tag{A.4}$$

$$\mathbf{v}_{0\perp i} = \mathbf{v}_{\mathbf{E}\times\mathbf{B}} + \mathbf{v}_{\star i} \tag{A.5}$$

where $\mathbf{v}_{\mathbf{E}\times\mathbf{B}} = -\nabla\phi \times \hat{\mathbf{b}}_0/B$ and $\mathbf{v}_{\star,i} = -\nabla p_i \times \hat{\mathbf{b}}_0/(Z_i e n_i B)$. The polarization drift is obtained from

$$\mathbf{v}_{\mathrm{pol},i} = \frac{\hat{\mathbf{b}}_0}{Z_i e n_i B} \times \frac{\mathrm{d}}{\mathrm{d}t}(m_i n_i \mathbf{v}_{0\perp i}) + \frac{\hat{\mathbf{b}}_0 \times m\mathbf{v}_{0\perp i} \nabla \cdot \mathbf{v}_{0i}}{Z_i e B} + \frac{\hat{\mathbf{b}}_0 \times \nabla \cdot \Pi_i}{Z_i e n_i B}. \tag{A.6}$$

The 0th order perpendicular velocity, crossed with the unit magnetic field, gives

$$\hat{\mathbf{b}}_0 \times n_i \mathbf{v}_{0\perp i} = -\left[\frac{n_i \nabla_\perp \phi}{B} + \frac{\nabla_\perp p_i}{B}\right], \tag{A.7}$$

while the divergence of $v_{\perp 0}$ is

$$\nabla \cdot \mathbf{v}_{0\perp i} \approx \frac{1}{B}\left[\left(\nabla \times \hat{\mathbf{b}}_0\right) \cdot \nabla\phi - \frac{\nabla B}{B} \cdot \hat{\mathbf{b}}_0 \times \nabla_\perp \phi\right] + \nabla_\parallel v_{\parallel i} + \frac{1}{Z_i e n_i B}\left[\left(\nabla \times \hat{\mathbf{b}}_0\right) \cdot \nabla p_i - \left(\frac{\nabla B}{B} + \frac{\nabla n_i}{n_i}\right) \cdot \hat{\mathbf{b}}_0 \times \nabla_\perp p_i\right], \tag{A.8}$$

where we assume a large aspect ratio tokamak, neglecting some small curvature terms $\sim \nabla \cdot \hat{\mathbf{b}}_0$.

The ion stress tensor is split into viscous and finite Larmor radius components in the same way it is treated in Ref. [14]:

$$\nabla \cdot \Pi_i = \nabla \cdot \Pi_{i,FLR} + \nabla \cdot \Pi_{i,vis}, \tag{A.9}$$

$$\nabla \cdot \Pi_{i,FLR} = -m_i n_i v_{\star i} \cdot \nabla \mathbf{v}_{0\perp i} + p_i \left(\nabla \times \frac{\hat{\mathbf{b}}_0}{\omega_{ci}}\right) \cdot \nabla \mathbf{v}_{0\perp i} + \nabla_\perp \left[\frac{p_i}{2\omega_{ci}} \nabla \cdot \left(\hat{\mathbf{b}}_0 \times \mathbf{v}_{0\perp i}\right)\right] + \hat{\mathbf{b}}_0 \times \nabla \left(\frac{p_i}{2\omega_{ci}} \nabla_\perp \cdot \mathbf{v}_{0\perp i}\right), \tag{A.10}$$

$$\nabla \cdot \Pi_{i,vis} = G_i \kappa - \frac{1}{3} \nabla G_i + \left[\nabla_\parallel G_i\right] \hat{\mathbf{b}}_0. \tag{A.11}$$

G_i is defined in equation (23). The last term of equation (A.8) multiplied by $\hat{\mathbf{b}}_0 \times n_i \mathbf{v}_{0\perp i}$, together with the first term of equation (A.10) cancel out the diamagnetic convection of the momentum in the total time derivative, as typically found when using the Braginskii closure. Hence, neglecting the polarization velocity from the convective derivative, the time derivative becomes $\frac{\mathrm{d}_i}{\mathrm{d}t} = \partial_t + \mathbf{v}_{\mathbf{E}\times\mathbf{B}} \cdot \nabla + v_{\parallel i} \hat{\mathbf{b}} \cdot \nabla$. This is not the case when more general closures are used, a discussion on the validity of the diamagnetic cancellation can be found in [48].

It is straightforward to show that, in the large aspect ratio limit, the rest of the terms stemming from $\hat{\mathbf{b}}_0 \times m\mathbf{v}_{0\perp i}(\nabla \cdot \mathbf{v}_{0i})/(Z_i e B)$ can be neglected. As the divergence of the velocity involves the magnetic field curvature, these terms are estimated to be a factor of ρ_s/R smaller than $\hat{\mathbf{b}}_0 \times \frac{\mathrm{d}}{\mathrm{d}t}(m_i n_i \mathbf{v}_{0\perp i})/(Z_i e n_i B)$.

The final expression for the polarization velocity (i.e. equation (15)) is

$$\mathbf{v}_{\mathrm{pol},i} \approx -\frac{1}{n_i \omega_{ci}} \frac{\mathrm{d}_i}{\mathrm{d}t}\left(\frac{n_i}{B} \nabla_\perp \phi + \frac{1}{B} \nabla_\perp p_i\right) + \frac{1}{m_i n_i \omega_{ci}} \hat{\mathbf{b}}_0 \times \left[G_i \kappa - \frac{\nabla G_i}{3}\right]. \tag{A.12}$$

The vorticity equation involves the divergence of the polarization current $j_{\mathrm{pol},i} = n_i \mathbf{v}_{\mathrm{pol},i}$. After some algebra, assuming a static magnetic field and again ordering curvature terms as R^{-1}, the following useful expressions are obtained

$$\omega = n_i \nabla_\perp \phi + \nabla_\perp p_i \tag{A.13}$$

$$\Omega = \nabla \cdot \omega \tag{A.14}$$

$$\nabla \cdot j_{\mathrm{pol},i} \approx -\frac{1}{B\omega_{ci}} \frac{\partial \Omega}{\partial t} - \frac{1}{B\omega_{ci}} \nabla \cdot \left[\nabla_\parallel (v_{\parallel i} \omega)\right] - \frac{1}{B\omega_{ci}} \nabla \cdot \left[\frac{\hat{\mathbf{b}}_0 \times \nabla_\perp \phi}{B} \cdot \nabla \omega\right] + \frac{1}{3 m_i \omega_{ci}} \hat{C}(G_i). \tag{A.15}$$

Equation (A.15), together with the divergence of the diamagnetic and parallel currents, leads directly to Equation (18).

References

[1] A. Loarte, B. Lipschultz, A. Kukushkin, G. Matthews, P. Stangeby, N. Asakura, G. Counsell, G. Federici, A. Kallenbach, K. Krieger, A. Mahdavi, V. Philipps, D. Reiter, J. Roth, J. Strachan, D. Whyte, R. Doerner, T. Eich, W. Fundamenski, A. Herrmann, M. Fenstermacher, P. Ghendrih, M. Groth, A. Kirschner, S. Konoshima, B. LaBombard, P. Lang, A. Leonard, P. Monier-Garbet, R. Neu, H. Pacher, B. Pegourie, R. Pitts, S. Takamura, J. Terry, E. Tsitrone, the ITPA Scrape-off Layer, D.P.T. Group, Chapter 4: Power and particle control, Nucl. Fusion 47 (2007) S203.

[2] S.J. Zweben, J.A. Boedo, O. Grulke, C. Hidalgo, B. LaBombard, R.J. Maqueda, P. Scarin, J.L. Terry, Edge turbulence measurements in toroidal fusion devices, Plasma Phys. Control. Fusion 49 (2007) S1.

[3] Y. Sarazin, P. Ghendrih, G. Attuel, C. Clément, X. Garbet, V. Grandgirard, M. Ottaviani, S. Benkadda, P. Beyer, N. Bian, C. Figarella, Theoretical understanding of turbulent transport in the sol, J. Nucl. Mater. 313 (2003) 796–803.

[4] V. Naulin, A.H. Nielsen, Accuracy of spectral and finite difference schemes in 2d advection problems, SIAM J. Sci. Comput. 25 (2003) 104–126.

[5] O.E. Garcia, V. Naulin, A.H. Nielsen, J.J. Rasmussen, Computations of intermittent transport in scrape-off layer plasmas, Phys. Rev. Lett. 92 (2004) 165003.
[6] J.R. Myra, D.A. Russell, D.A. D'Ippolito, J.-W. Ahn, R. Maingi, R.J. Maqueda, D.P. Lundberg, D.P. Stotler, S.J. Zweben, J. Boedo, M. Umansky, N. Team, Reduced model simulations of the scrape-off-layer heat-flux width and comparison with experiment, Phys. Plasmas 18 (2011) 012305.
[7] D.A. Russell, J.R. Myra, D.A. D'Ippolito, T.L. Munsat, Y. Sechrest, R.J. Maqueda, D.P. Stotler, S.J. Zweben, the NSTX team, Comparison of scrape-off layer turbulence simulations with experiments using a synthetic gas puff imaging diagnostic, Phys. Plasmas 18 (2011) 022306.
[8] S.I. Krasheninnikov, D.A. D'Ippolito, J.R. Myra, Recent theoretical progress in understanding coherent structures in edge and SOL turbulence, J. Plasma Phys. 74 (2008) 679–717.
[9] B.D. Scott, Drift wave versus interchange turbulence in tokamak geometry: linear versus nonlinear mode structure, Phys. Plasmas 12 (2005) 062314.
[10] T.T. Ribeiro, B. Scott, Gyrofluid turbulence studies of the effect of the poloidal position of an axisymmetric Debye sheath, Plasma Phys. Control. Fusion 50 (2008) 055007.
[11] B. Dudson, M. Umansky, X. Xu, P. Snyder, H. Wilson, BOUT++: a framework for parallel plasma fluid simulations, Comput. Phys. Commun. 180 (2009) 1467–1480.
[12] P. Tamain, P. Ghendrih, E. Tsitrone, V. Grandgirard, X. Garbet, Y. Sarazin, E. Serre, G. Ciraolo, G. Chiavassa, Tokam-3d: a 3d fluid code for transport and turbulence in the edge plasma of tokamaks, J. Comput. Phys. 229 (2010) 361–378.
[13] P. Tamain, P. Ghendrih, H. Bufferand, G. Ciraolo, C. Colin, N. Fedorczak, N. Nace, F. Schwander, E. Serre, Multi-scale self-organisation of edge plasma turbulent transport in 3d global simulations, Plasma Phys. Control. Fusion 57 (2015) 054014.
[14] P. Ricci, F.D. Halpern, S. Jolliet, J. Loizu, A. Mosetto, A. Fasoli, I. Furno, C. Theiler, Simulation of plasma turbulence in scrape-off layer conditions: the GBS code, simulation results and code validation, Plasma Phys. Control. Fusion 54 (2012) 124047.
[15] A. Fasoli, B. Labit, M. McGrath, S.H. Muller, G. Plyushchev, M. Podesta, F.M. Poli, Electrostatic turbulence and transport in a simple magnetized plasma, Phys. Plasmas 13 (2006) 055902.
[16] P. Ricci, B.N. Rogers, S. Brunner, High- and low-confinement modes in simple magnetized toroidal plasmas, Phys. Rev. Lett. 100 (2008) 225002.
[17] A. Arakawa, Computational design for long-term numerical integration of the equations of fluid motion: two-dimensional incompressible flow. Part I, J. Comput. Phys. 1 (1966) 119–143.
[18] J.W. Connor, R.J. Hastie, J.B. Taylor, Shear, periodicity, and plasma ballooning modes, Phys. Rev. Lett. 40 (1978) 396–399.
[19] S. Jolliet, F.D. Halpern, J. Loizu, A. Mosetto, P. Ricci, Aspect ratio effects on limited scrape-off layer plasma turbulence, Phys. Plasmas 21 (2014) 022303.
[20] S. Jolliet, F. Halpern, J. Loizu, A. Mosetto, F. Riva, P. Ricci, Numerical approach to the parallel gradient operator in tokamak scrape-off layer turbulence simulations and application to the GBS code, Comput. Phys. Commun. 188 (2015) 21–32.
[21] A. Mosetto, F.D. Halpern, S. Jolliet, J. Loizu, P. Ricci, Finite ion temperature effects on scrape-off layer turbulence, Phys. Plasmas 22 (2015).
[22] C. Wersal, P. Ricci, A first-principles self-consistent model of plasma turbulence and kinetic neutral dynamics in the tokamak scrape-off layer, Nucl. Fusion 55 (2015) 123014.
[23] S. Coda, the TCV Team, The science program of the TCV tokamak: exploring fusion reactor and power plant concepts, Nucl. Fusion 55 (2015) 104004.
[24] M. Greenwald, A. Bader, S. Baek, H. Barnard, W. Beck, W. Bergerson, I. Bespamyatnov, M. Bitter, P. Bonoli, M. Brookman, D. Brower, D. Brunner, W. Burke, J. Candy, M. Chilenski, M. Chung, M. Churchill, I. Cziegler, E. Davis, G. Dekow, L. Delgado-Aparicio, A. Diallo, W. Ding, A. Dominguez, R. Ellis, P. Ennever, D. Ernst, I. Faust, C. Fiore, E. Fitzgerald, T. Fredian, O. Garcia, C. Gao, M. Garrett, T. Golfinopoulos, R. Granetz, R. Groebner, S. Harrison, R. Harvey, Z. Hartwig, K. Hill, J. Hillairet, N. Howard, A. Hubbard, J. Hughes, I. Hutchinson, J. Irby, A. James, A. Kanojia, C. Kasten, J. Kesner, C. Kessel, R. Kube, B. LaBombard, C. Lau, J. Lee, K. Liao, Y. Lin, B. Lipschultz, Y. Ma, E. Marmar, P. McGibbon, O. Meneghini, D. Mikkelsen, D. Miller, R. Mumgaard, R. Murray, R. Ochoukov, G. Olynyk, D. Pace, S. Park, R. Parker, Y. Podpaly, M. Porkolab, M. Preynas, I. Pusztai, M. Reinke, J. Rice, W. Rowan, S. Scott, S. Shiraiwa, J. Sierchio, P. Snyder, B. Sorbom, V. Soukhanovskii, J. Stillerman, L. Sugiyama, C. Sung, D. Terry, J. Terry, C. Theiler, N. Tsujii, R. Vieira, J. Walk, G. Wallace, A. White, D. Whyte, J. Wilson, S. Wolfe, K. Woller, G. Wright, J. Wright, S. Wukitch, G. Wurden, P. Xu, C. Yang, S. Zweben, Overview of experimental results and code validation activities at Alcator C-Mod, Nucl. Fusion 53 (2013) 104004.
[25] A. Zeiler, J.F. Drake, B. Rogers, Nonlinear reduced Braginskii equations with ion thermal dynamics in toroidal plasma, Phys. Plasmas 4 (1997) 2134–2138.
[26] B.N. Rogers, P. Ricci, Low-frequency turbulence in a linear magnetized plasma, Phys. Rev. Lett. 104 (2010) 225002.
[27] D.M. Fisher, B.N. Rogers, G.D. Rossi, D.S. Guice, Three-dimensional two-fluid Braginskii simulations of the large plasma device, Phys. Plasmas 22 (2015).
[28] P. Ricci, B.N. Rogers, Transport scaling in interchange-driven toroidal plasmas, Phys. Plasmas 16 (2009) 062303.
[29] P. Ricci, B.N. Rogers, Turbulence phase space in simple magnetized toroidal plasmas, Phys. Rev. Lett. 104 (2010) 145001.
[30] P. Ricci, C. Theiler, A. Fasoli, I. Furno, K. Gustafson, D. Iraji, J. Loizu, Methodology for turbulence code validation: quantification of simulation-experiment agreement and application to the TORPEX experiment, Phys. Plasmas 18 (2011) 032109.
[31] F.D. Halpern, A. Cardellini, P. Ricci, S. Jolliet, J. Loizu, A. Mosetto, Three-dimensional simulations of blob dynamics in a simple magnetized torus, Phys. Plasmas 21 (2014) 022305.
[32] P. Ricci, F. Riva, C. Theiler, A.F. Fasoli, I. Furno, F.D. Halpern, J. Loizu, Approaching the investigation of plasma turbulence through a rigorous verification and validation procedure: a practical example, Phys. Plasmas 22 (2015) 055704.
[33] P. Ricci, B.N. Rogers, Plasma turbulence in the scrape-off layer of tokamak devices, Phys. Plasmas 20 (2013) 010702.
[34] J. Loizu, P. Ricci, F.D. Halpern, S. Jolliet, Boundary conditions for plasma fluid models at the magnetic presheath entrance, Phys. Plasmas 19 (2012) 122307.
[35] A. Mosetto, F.D. Halpern, S. Jolliet, P. Ricci, Low-frequency linear-mode regimes in the tokamak scrape-off layer, Phys. Plasmas 19 (2012) 112103.
[36] A. Mosetto, F.D. Halpern, S. Jolliet, J. Loizu, P. Ricci, Turbulent regimes in the tokamak scrape-off layer, Phys. Plasmas 20 (2013) 092308.
[37] J. Loizu, P. Ricci, F.D. Halpern, S. Jolliet, A. Mosetto, On the electrostatic potential in the scrape-off layer of magnetic confinement devices, Plasma Phys. Control. Fusion 55 (2013) 124019.
[38] J. Loizu, P. Ricci, F.D. Halpern, S. Jolliet, A. Mosetto, Intrinsic toroidal rotation in the scrape-off layer of tokamaks, Phys. Plasmas 21 (2014) 062309.
[39] J. Loizu, P. Ricci, F. Halpern, S. Jolliet, A. Mosetto, Effect of the limiter position on the scrape-off layer width, radial electric field and intrinsic flows, Nucl. Fusion 54 (2014) 083033.
[40] F.D. Halpern, S. Jolliet, J. Loizu, A. Mosetto, P. Ricci, Ideal ballooning modes in the tokamak scrape-off layer, Phys. Plasmas 20 (2013) 052306.
[41] F.D. Halpern, J.L. Terry, S.J. Zweben, B. LaBombard, M. Podesta, P. Ricci, Theory-based scaling of the SOL width in circular limited tokamak plasmas, Nucl. Fusion 53 (2013) 122001.
[42] F. Halpern, P. Ricci, S. Jolliet, J. Loizu, A. Mosetto, Theory of the scrape-off layer width in inner-wall limited tokamak plasmas, Nucl. Fusion 54 (2014) 043003.
[43] S.J. Zweben, B.D. Scott, J.L. Terry, B. LaBombard, J.W. Hughes, D.P. Stotler, Comparison of scrape-off layer turbulence in Alcator C-Mod with three dimensional gyrofluid computations, Phys. Plasmas 16 (2009) 082505.
[44] F. Halpern, et al., Comparison of 3D flux-driven scrape-off layer turbulence simulations with gas-puff imaging of Alcator C-Mod inner wall limited discharges, Plasma Phys. Control. Fusion 57 (2015) 054005.
[45] H.P. Summers, W.J. Dickson, M.G. O'Mullane, N.R. Badnell, A.D. Whiteford, D.H. Brooks, J. Lang, S.D. Loch, D.C. Griffin, Ionization state, excited populations and emission of impurities in dynamic finite density plasmas: I. The generalized collisional-radiative model for light elements, Plasma Phys. Control. Fusion 48 (2006) 263.

[46] S.I. Braginskii, Transport processes in a plasma, Reviews of Plasma Physics, vol. 1, Consultants Bureau, New York, 1965.
[47] P. Helander, D. Sigmar, Collisional Transport in Magnetized Plasmas, Cambridge Monographs on Plasma Physics, Cambridge University Press, 2005.
[48] J.J. Ramos, General expression of the gyroviscous force, Phys. Plasmas 12 (2005) 112301.
[49] A.N. Simakov, P.J. Catto, Drift-ordered fluid equations for field-aligned modes in low-β collisional plasma with equilibrium pressure pedestals, Phys. Plasmas 10 (2003) 4744–4757.
[50] A.N. Simakov, P.J. Catto, Erratum: "Drift-ordered fluid equations for field-aligned modes in low-β collisional plasma with equilibrium pressure pedestals" [Phys. Plasmas 10 (2003) 4744], Phys. Plasmas 11 (2004) 2326.
[51] K.U. Riemann, The Bohm criterion and sheath formation, J. Phys. D, Appl. Phys. 24 (1991) 493.
[52] A.M. Dimits, G. Bateman, M.A. Beer, B.I. Cohen, W. Dorland, G.W. Hammett, C. Kim, J.E. Kinsey, M. Kotschenreuther, A.H. Kritz, L.L. Lao, J. Mandrekas, W.M. Nevins, S.E. Parker, A.J. Redd, D.E. Shumaker, R. Sydora, J. Weiland, Comparisons and physics basis of tokamak transport models and turbulence simulations, Phys. Plasmas 7 (2000) 969–983.
[53] W.L. Oberkampf, C.J. Roy, Verification and Validation in Scientific Computing, Cambridge University Press, 2010.
[54] F. Riva, P. Ricci, F.D. Halpern, S. Jolliet, J. Loizu, A. Mosetto, Verification methodology for plasma simulations and application to a scrape-off layer turbulence code, Phys. Plasmas 21 (2014) 062301.
[55] I. Wolfram Research, Mathematica, version 8.0 ed., Wolfram Research, Inc., Champaign, Illinois, 2010.
[56] Y. Marandet, A. Mekkaoui, D. Reiter, P. Börner, P. Genesio, F. Catoire, J. Rosato, H. Capes, L. Godbert-Mouret, M. Koubiti, R. Stamm, Transport of neutral particles in turbulent scrape-off layer plasmas, Nucl. Fusion 51 (2011) 083035.
[57] W. Briggs, V. Henson, S. McCormick, A Multigrid Tutorial, second edition, Society for Industrial and Applied Mathematics, 2000.
[58] U. Trottenberg, A. Schuller, Multigrid, Academic Press, Inc., Orlando, FL, USA, 2001.
[59] P.R. Amestoy, I.S. Duff, J. Koster, J.-Y. L'Excellent, A fully asynchronous multifrontal solver using distributed dynamic scheduling, SIAM J. Matrix Anal. Appl. 23 (2001) 15–41.
[60] P.R. Amestoy, A. Guermouche, J.-Y. L'Excellent, S. Pralet, Hybrid scheduling for the parallel solution of linear systems, Parallel Comput. 32 (2006) 136–156.
[61] O. Schenk, A. Wächter, M. Hagemann, Matching-based preprocessing algorithms to the solution of saddle-point problems in large-scale nonconvex interior-point optimization, Comput. Optim. Appl. 36 (2007) 321–341.
[62] J. Madsen, O.E. Garcia, J.S. Larsen, V. Naulin, A.H. Nielsen, J.J. Rasmussen, The influence of finite Larmor radius effects on the radial interchange motions of plasma filaments, Phys. Plasmas 18 (2011) 112504.
[63] P. Manz, G. Birkenmeier, D. Carralero, G. Fuchert, H.W. Müller, S.H. Müller, B.D. Scott, U. Stroth, T.T. Ribeiro, E. Wolfrum, The influence of finite ion temperature on plasma blob dynamics, Plasma Phys. Control. Fusion 57 (2015) 014012.
[64] A. Kendl, Inertial blob-hole symmetry breaking in magnetised plasma filaments, Plasma Phys. Control. Fusion 57 (2015) 045012.
[65] F. Riva, C. Colin, J. Denis, L. Easy, I. Furno, J. Madsen, F. Militello, V. Naulin, A.H. Nielsen, J.M.B. Olsen, J.T. Omotani, J.J. Rasmussen, P. Ricci, E. Serre, P. Tamain, C. Theiler, Blob dynamics in the TORPEX experiment: a multi-code validation, Plasma Phys. Control. Fusion 58 (2016) 044005.
[66] H. Meyer, I. Abel, R. Akers, A. Allan, S. Allan, L. Appel, O. Asunta, M. Barnes, N. Barratt, N.B. Ayed, J. Bradley, J. Canik, P. Cahyna, M. Cecconello, C. Challis, I. Chapman, D. Ciric, G. Colyer, N. Conway, M. Cox, B. Crowley, S. Cowley, G. Cunningham, A. Danilov, A. Darke, M.D. Bock, G.D. Temmerman, R. Dendy, P. Denner, D. Dickinson, A. Dnestrovsky, Y. Dnestrovsky, M. Driscoll, B. Dudson, D. Dunai, M. Dunstan, P. Dura, S. Elmore, A. Field, G. Fishpool, S. Freethy, W. Fundamenski, L. Garzotti, Y. Ghim, K. Gibson, M. Gryaznevich, J. Harrison, E. Havlíčková, N. Hawkes, W. Heidbrink, T. Hender, E. Highcock, D. Higgins, P. Hill, B. Hnat, M. Hole, J. Horáček, D. Howell, K. Imada, O. Jones, E. Kaveeva, D. Keeling, A. Kirk, M. Kocan, R. Lake, M. Lehnen, H. Leggate, Y. Liang, M. Lilley, S. Lisgo, Y. Liu, B. Lloyd, G. Maddison, J. Mailloux, R. Martin, G. McArdle, K. McClements, B. McMillan, C. Michael, F. Militello, P. Molchanov, S. Mordijck, T. Morgan, A. Morris, D. Muir, E. Nardon, V. Naulin, G. Naylor, A. Nielsen, M. O'Brien, T. O'Gorman, S. Pamela, F. Parra, A. Patel, S. Pinches, M. Price, C. Roach, J. Robinson, M. Romanelli, V. Rozhansky, S. Saarelma, S. Sangaroon, A. Saveliev, R. Scannell, J. Seidl, S. Sharapov, A. Schekochihin, V. Shevchenko, S. Shibaev, D. Stork, J. Storrs, A. Sykes, G. Tallents, P. Tamain, D. Taylor, D. Temple, N. Thomas-Davies, A. Thornton, M. Turnyanskiy, M. Valovič, R. Vann, E. Verwichte, P. Voskoboynikov, G. Voss, S. Warder, H. Wilson, I. Wodniak, S. Zoletnik, R. Zagôrski, the MAST and NBI teams, Overview of physics results from MAST towards ITER/DEMO and the MAST upgrade, Nucl. Fusion 53 (2013) 104008.
[67] M. Kocan, R. Pitts, G. Arnoux, I. Balboa, P. de Vries, R. Dejarnac, I. Furno, R. Goldston, Y. Gribov, J. Horacek, M. Komm, B. Labit, B. LaBombard, C. Lasnier, R. Mitteau, F. Nespoli, D. Pace, R. Panek, P. Stangeby, J. Terry, C. Tsui, P. Vondracek, Impact of a narrow limiter SOL heat flux channel on the ITER first wall panel shaping, Nucl. Fusion 55 (2015) 033019.
[68] P. Tamain, P. Ghendrih, E. Tsitrone, Y. Sarazin, X. Garbet, V. Grandgirard, J. Gunn, E. Serre, G. Ciraolo, G. Chiavassa, 3d modelling of edge parallel flow asymmetries, in: Proceedings of the 18th International Conference on Plasma–Surface Interactions in Controlled Fusion Device, J. Nucl. Mater. 390–391 (2009) 347–350.